https://doi.org/10.5194/egusphere-2026-2699
Preprint. Discussion started: 29 May 2026

Bioaerosols outcompete dust as dominant immersion-mode-INPs in central Europe and redefine INP parameterizations

Kunfeng Gao[1,†,*], Romanos Foskinis[1,2], Marilena Gidarakou[3], Kalliopi Violaki[1], Guangyu Li[4,‡], Benjamin Tobias Brem[5], Sophie Erb[6], Bernard Clot[6], Marie-José Graber[6], Branko Sikoparjja[7], Predrag Matavulja[8], Dusan Licina[9], Cuiqi Zhang[4], Benoît Crouzy[6], Alexandros Papayannis[1,3], Zamin A. Kanji[4] and Athanasios Nenes[1,10*]

[1]Laboratory of Atmospheric Processes and Their Impacts, School of Architecture, Civil and Environmental Engineering, École Polytechnique Fédérale de Lausanne, Lausanne, Switzerland.
[2]Environmental Remote Sensing Laboratory, School of Architecture, Civil and Environmental Engineering, École Polytechnique Fédérale de Lausanne, Lausanne, Switzerland.
[3]Laser Remote Sensing Unit, Physics Department, National Technical University of Athens, Zografou, Greece.
[4]Department of Environmental Systems Science, Institute for Atmospheric and Climate Science, ETH Zurich, Zurich, Switzerland.
[5]PSI Center for Energy and Environmental Sciences, Villigen PSI, Switzerland.
[6]Federal Office of Meteorology and Climatology MeteoSwiss, Payerne, Switzerland.
[7]Biosense Institute - Research and Development Institute for Information Technologies in Biosystems, University of Novi Sad, Novi Sad, Serbia
[8]Institute for Data Science, University of Applied Sciences North – Western Switzerland, Bahnhofstrasse 6, Windisch, Switzerland
[9]Human-Oriented Built Environment Lab, School of Architecture, Civil and Environmental Engineering, École Polytechnique Fédérale de Lausanne, Lausanne, Switzerland.
[10]Centre for Studies of Air Quality and Climate Change, Institute of Chemical Engineering Sciences, Foundation for Research and Technology Hellas, Patras, Greece.
[†]Present address: Department of Environmental Systems Science, Institute for Atmospheric and Climate Science, ETH Zurich, Zurich, Switzerland
[‡]Present address: Laboratory for Microwave Spatial Intelligence and Cloud Platform, Deqing Academy of Satellite Applications, Deqing, China

Correspondence to: Athanasios Nenes (athanasios.nenes@epfl.ch) and Kunfeng Gao (kunfeng.gao@env.ethz.ch)

Abstract.

Knowledge gaps in the source and parameterization of ice-nucleating particles (INPs) remain a major uncertainty in quantifying the properties and climate impacts of mixed-phase clouds (MPCs). Bioaerosols are increasingly recognized as important INPs for MPCs, yet it is unclear whether their contribution is critical through modelling studies. We investigate this using field observations at a semi-rural site in the central Europe, combining INP and aerosol measurements, remote sensing, and air-mass source analysis. We synergically use the results of in-situ and offline measurements to identify INPs originated from different sources, including biological aerosols, dust, and biomass burning aerosols, and to quantify their abundance and relative contributions to total INPs. More than 85% of immersion-mode INPs (>−24°C) are heat-labile and significantly correlated with fluorescent biological aerosols particles and pollen, while heat-resistant INPs (<~10%) are likely mineral dust, while biomass burning is an insignificant source. The proposed bioaerosol-ware INP parameterization reproduces observations across multi-regional datasets, showing that neglecting bioaerosol-INPs results in an average ~50%

https://doi.org/10.5194/egusphere-2026-2699
Preprint. Discussion started: 29 May 2026

(~32%) bias in predictions of immersion-mode INPs active warmer than −15°C (−24°C), with frequent deviations of up to an order of magnitude from observations.

1 Introduction

The largest source of uncertainty regarding cloud impacts on climate is related to low clouds, largely stemming from uncertainties in processes that affect their life time (Mülmenstädt et al., 2021), glaciation state (Lohmann, 2002) and optical thickness (Mccoy et al., 2016) in which the cloud phase plays a key role (Korolev and Milbrandt, 2022). Mixed-phase clouds (MPCs) consist of both ice crystals and supercooled water droplets, leading to their thermodynamically unstable states (Lohmann, 2002) and thus highly uncertain radiation forcing. For example, orographic MPCs enhanced by secondary ice production can exert a profound impact on regional precipitation and thus hydrological cycle (Georgakaki et al., 2024). Notably, MPCs are ubiquitous and persistent in the Arctic (Morrison et al., 2011) and over orographic terrains (Lohmann et al., 2016), regions where climate change exerts amplified effects on land cover and aerosol sources. These changes, in turn, regulate MPC formation.

MPCs exist over a wide temperature (T) range (0 to −38°C), spanning large volumes of the troposphere, where ice cannot form via homogeneous freezing of cloud droplets but instead depends on the availability of ice nucleating particles (INPs) that initiate heterogeneous ice nucleation (IN, e.g., immersion-mode freezing) (Pruppacher and Klett, 2010) and may subsequently trigger secondary ice production (Korolev and Leisner, 2020). As such, INPs play a key role in regulating the phase of MPCs. In the atmosphere, INPs can originate from different sources (Kanji et al., 2017), including mineral dust particles from deserts (Brunner et al., 2021; Gao et al., 2024), soil dust (Steinke et al., 2016; O'sullivan et al., 2013), marine organics and sea spray aerosols, volcanic ash, biomass burning aerosols from wildfires and/or anthropogenic fuel uses, as well as primary biological aerosol particles (PBAPs) from ecosystems (Tobo et al., 2013; Schneider et al., 2021; Gao et al., 2024). It is reported that PBAPs play a dominant role for the ice formation in MPCs with T>−15°C (Coluzza et al., 2017; Cornwell et al., 2023; O'sullivan et al., 2018) where secondary ice production also occurs and can be strongly amplified, while dust generally acts as INPs at lower temperatures (Murray et al., 2012; Kanji et al., 2017). For instance, based on both simulation results and field observations, Georgakaki et al. (2024) reported that primary ice formation induced by active INPs from PBAPs (Gao et al., 2024) prolifically catalysed secondary ice production through ice-ice collisional break-up (Phillips et al., 2017) ultimately leading to enhanced precipitation. At T>−10°C, the very limited IN activity of nonbiological particles allow PBAPs, together with secondary ice production, to become a key driver of MPC glaciation. However, only a few studies considered PBAPs and associated secondary ice production in climate models (Patade et al., 2022; Hoose et al., 2010; Georgakaki et al., 2024).

Several studies have reported the dominant contribution of PBAPs to INPs in the MPC regime. For example, the significant correlations between PBAPs and immersion-mode INPs were observed at a mountain top in the eastern Mediterranean (Gao et al., 2024), in a forest ecosystem in the Central Rocky Mountains (Tobo et al., 2013), and at an Arctic mountain site

https://doi.org/10.5194/egusphere-2026-2699
Preprint. Discussion started: 29 May 2026

(Pereira Freitas et al., 2023). Prenni et al. (2009) reported the primary and secondary INP contributions from local PBAPs and Saharan dust in the Amazon basin. Schneider et al. (2021) found the seasonal cycle of INPs is linked to the abundance of PBAPs in boreal forests. Cornwell et al. (2023) identified bioaerosols as the primary source of INPs between −12 and −20°C in the coastal California. However, owing to strong regional and seasonal variability in PBAPs and INPs, they are poorly represented in existing models (Cornwell et al., 2023; Tobo et al., 2013). Yet, models that explicitly simulate PBAP cycles are now emerging (Chatziparaschos et al., 2025), enabling the development and application of PBAP-based INP parameterizations. To further improve the representation of PBAPs in models, comprehensive datasets including major PBAP types and robust, transferable parameterizations linking PBAPs to INPs across regions are still lacking (Patade et al., 2022). In this study, we conducted a field campaign at a semi-rural site on the Swiss Plateau (491 m above sea level, a.s.l.) in central Europe where MPCs persistently exist (Lohmann et al., 2016), from May to December 2023, to quantify the contribution of PBAPs to immersion-mode INPs, to investigate the relative importance of PBAPs versus dust, and to parameterize PBAP IN activity in MPCs for modelling applications. We then apply the parameterization across multi-regional datasets and assess its universality and the importance of including PBAP INPs.

2 Measurement setup and methodology

2.1 Measurement site

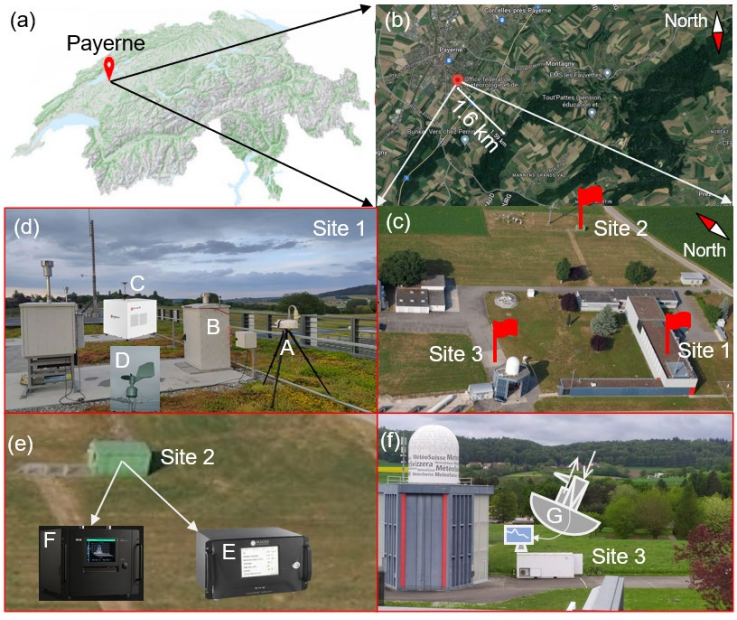

Figure 1. Overview of the instrumentation setup for PERICLES campaign. (a) The location of MeteoSwiss station at Payerne, Switzerland. (b) Satellite aerial view of the station (Google map). (c) The top view of the station and the location of three observation sites. (d) Site 1 for Coriolis aerosol sampler (A), Wideband Integrated Bioaerosol Sensor (WIBS, B), Rapid-E (C) and Hirst (D). (e) Site 2 for total carbon analyzer (E) and aethalometer (F). (f) Site 3 for remote sensing measurements using a UV-Fluorescent-Mie lidar (G) to observe the spatio-temporal evolution of aerosol particles.

https://doi.org/10.5194/egusphere-2026-2699
Preprint. Discussion started: 29 May 2026

A field campaign, called PayernE lidaR Insitu detection of fluorescent biomass burning, bioaerosol and dust partiCLES and their cloud impacts (PERICLES), was conducted at the Payerne MeteoSwiss station (46.822° N, 6.941° E, 491 m a.s.l.) on the Swiss Plateau, from 8 May to 8 December 2023. The site is located at a semi-rural area surrounded by grassland and several farmlands and is close to a forest ecosystem (~1.6 km south-east from the station, Fig. 1b). A suite of in-situ online and offline instruments, as well as remote sensing measurements, was combined to monitor the aerosol properties and to measure INP concentration values (N_{INP}). The instruments were deployed at three measurement sites as shown in Fig. 1c. The Site 1 is at the roof terrace of a two-story building, where a wet cyclone aerosol sampler (A), Wideband Integrated Bioaerosol Sensor (WIBS, B), Rapid-E (C) and Hirst (D) were employed to collect aerosols for offline INP measurements (A) and to monitor fluorescent biological aerosol particles (FBAPs, B) and plant pollen (C and D). An aethalometer (E) used for elemental carbon analysis and a total carbon analyser (F) were installed at Site 2 which is approximately 70 m south-west from Site 1. Additionally, a UV-Fluorescent-Mie lidar system (G) was set up at Site 3 to obtain the vertical distribution of aerosol elastic and fluorescent backscatter coefficients (Gidarakou et al., 2026). We also ran HYbrid Single-Particle Lagrangian Integrated Trajectory (HYSPLIT) simulations to calculate the back trajectories of air-masses arriving at the measuring site and track the source of long-range transported aerosols.

2.2 INP measurements

Ambient aerosol was collected into ~15 ml ultrapure water (W4502-1L, Sigma-Aldrich, US) over a time span between 10 and 60 minutes using a high-flow-rate wet cyclone aerosol sampler (Coriolis® μ, Bertin Instruments, France, 300 L min^{-1}). The sampler collects particles between 0.5 and 20 μm and has a collection efficiency of 50%, 80%, and 94% for 0.5, 2.0, and 5.0μm particles, respectively (Wieder et al., 2022). Due to water vapor evaporation, the cyclone was refilled to 15 ml for every 10 min. For every aerosol sample, a corresponding background sample was prepared by collecting the blank ultrapure water, as described in David et al. (2019). Before immersion-mode INP analysis using an offline droplet freezing assay called DRoplet Ice Nuclei Counter Zurich (DRINCZ) (David et al., 2019), all samples were stored at −20°C for less than 2 months, suggested to be a proper practice to preserve INP samples (Beall et al., 2020). In total, 103 aerosol samples were tested. The sampling time and number ID of each sample are provided in Supplement Fig. S1 and Table S1, respectively. Fpr each sample, three DRINCZ experiments were conducted at three different dilutions with a dilution ratio from a factor of 10 to 100, to ensure more accurate detection of low concentration INPs. Also, 79 of the 103 samples were subjected to heating treatment at 90°C for 40 minutes prior to DRINCZ experiments (termed T90 samples), to quantify the contribution of heat-labile particles, such as proteins or biological macromolecules, to the INP population. Additionally, 28 background samples, representative of 28 sample collection batches, were analysed to correct background noise. For samples without a corresponding background test, a fitted background curve, as presented in Figs. S2 and S3 for untreated and T90 samples respectively, was calculated following the method in David et al. (2019). With background corrections, N_{INP} values as a function of T for each sample were obtained following the DRINCZ data processing protocol reported in Wieder et al. (2022). For untreated samples with different dilutions, the data was processed to calculate the combined weighted average

https://doi.org/10.5194/egusphere-2026-2699
Preprint. Discussion started: 29 May 2026

N_{INP} spectra (Wieder et al., 2022). Additionally, we tested the effect of temperature bin size (ΔT, 0.33, 0.5 and 1.0°C) used for raw data point resampling on the calculated N_{INP} results (Fig. S4) and note that a larger ΔT generally results in a smaller estimation of N_{INP}. In the main text, we present the N_{INP} results with a ΔT of 1.0°C as used by other DRINCZ users (Wieder et al., 2022; Li et al., 2023).

2.3 In-situ aerosol property measurements

2.3.1 Fluorescent biological aerosol particles

A Wideband Integrated Bioaerosol Sensor-New Electronics Option (WIBS-5/NEO, Droplet Measurement Technologies) was used to detect the real-time and size-resolved number concentration of fluorescent aerosol particles (0.5–30μm). WIBS was configured with an omnidirectional total inlet. WIBS utilizes pulsed ultraviolet light to excite fluorescence from individual particles and then detects the fluorescence emissions at two wavebands, resulting in three fluorescence detectors including FL1 (excitation at 280 nm and emission at 310–400 nm), FL2 (excitation at 280 nm and emission at 420–650 nm) and FL3 (excitation at 370 nm and emission at 420–650 nm) (Perring et al., 2015). The three fluorescence detectors are sensitive to tryptophan-containing proteins, NAD(P)H co-enzymes and riboflavin respectively which are frequently observed biological fluorophores (Savage et al., 2017). The instrument was operated in forced trigger mode every twelve hours for one minute. Particles detected by any one of three detectors are termed $Fluo_{WIBS}$; particles that show fluorescence in only one of three detectors are denoted as types A_{WIBS}, B_{WIBS} and C_{WIBS}, respectively; particles that exhibit only two types of fluorescence signals are named as types AB_{WIBS}, AC_{WIBS} and BC_{WIBS}, respectively; particles carrying three fluorophores are attributed to a type of ABC_{WIBS}. Among all types of particles, ABC_{WIBS} particles are of the highest probability of being biological in origin and thus representative of fluorescent biological aerosol particles (FBAPs) (Perring et al., 2015; Savage et al., 2017). A dynamic fluorescence threshold, defined as the mean background signal plus nine standard deviations (9σ), was applied to distinguish true particle fluorescence from instrumental noise (consistent with standard WIBS processing protocols). The threshold is also applied for all WIBS data used for INP parameterizations. WIBS also counts the number concentration of all aerosol particles larger than 0.5μm in optical size, termed $Total_{WIBS}$. The number concentrations of particles larger (smaller) than 2.5μm for the types of $Total_{WIBS}$ $Fluo_{WIBS}$ and ABC_{WIBS} were also calculated and termed $Total_{WIBS>2.5\mu m}$, $Fluo_{WIBS>2.5\mu m}$ and $ABC_{WIBS>2.5\mu m}$ ($ABC_{WIBS<2.5\mu m}$), respectively. Additionally, the difference between $Total_{WIBS>2.5\mu m}$ and $ABC_{WIBS>2.5\mu m}$ was attributed to $\Delta Coarse_{>2.5\mu m}$ and assumed as the upper limit of coarse-sized dust particles excluding coarse-sized PBAPs, such as pollen. Similarly, the difference between $Total_{WIBS>2.5\mu m}$ and $Fluo_{WIBS>2.5\mu m}$ was treated as a lower limit of coarse-sized dust particles termed $\Delta Coarse_{>2.5\mu m,nonFluo}$, considering that some mineral dust particles may show fluorescence (Morrison et al., 2020).

https://doi.org/10.5194/egusphere-2026-2699
Preprint. Discussion started: 29 May 2026

2.3.2 Pollen monitoring

Both a real-time automatic (Rapid-E) and a weekly-cycle manual (Hirst) pollen instruments were employed at Site 1 (Fig. 1d) to record hourly averaged pollen concentrations. Rapid-E (Plair SA, Geneva, Switzerland) uses a laser-fluorescence-based method to acquire both scattering and fluorescent data of single particles (Kiselev et al., 2013; Kiselev et al., 2011). The time-resolved scattering data, including the optical size and the particle shape, was recorded by photo-detectors monitoring the particle after passing through a 450 nm laser beam. In addition, the particle was excited by a second but more powerful laser beam (337 nm nitrogen laser) to obtain wavelength-resolved fluorescence spectra recorded by an array of 32 photo-detectors arranged within a spectral range of 350–800 nm. On the basis of the size, morphology and fluorescent property of the particles, the instrument can recognize the type of single pollen particles using automatic pollen recognition algorithms (Šaulienė et al., 2019; Chappuis et al., 2019; Crouzy et al., 2016). In this study, the number concentration of 11 types of pollen particles (10-100 μm) which were prevalent in the observation seasons was calculated and its sum was termed $RapidE_{Total}$. Following Tešendić et al. (2020), we use pollen classification algorithm based on convolutional neural network to allow automatic feature extraction from scattering light fluorescence spectrum and life time of fluorescence measurements of each particle sampled by Rapid-E. Pollen taxa detected by Rapid-E are provided in Supplement S5.

Hirst is a volumetric pollen trap and collects airborne particles on a rotating drum with adhesive slides, which serves as a standard method for pollen monitoring in Europe (Oteros et al., 2017; Hirst, 1952). The inlet (14 × 2 mm opening) of a Hirst-type sampler can be self-oriented towards the wind direction by a vane. The slides will be replaced once a week and then analysed by using microscopy to manually identify and count the number of 48 types of pollen particles larger than 10 μm (termed $Hirst_{Total}$). Hirst measurements provide standardized pollen identification (Standardization, 2019), albeit with limited time resolution due to the spreading on the band: the 2 mm opening corresponds to one hour of drum rotation. Pollen taxa detected by Hirst are provided in Supplement S6.

2.3.3 Particulate matter for eBC and coarse-sized dust particles

The mass concentration of elemental black carbon (eBC) from refractory and carbonaceous aerosol particles was recorded by an aethalometer (AE33, Magee Scientific, US) at 880 nm in real time. Using a total carbon analyser (Model TCA08, Aerosol Magee Scientific, US), the total mass of carbonaceous particle (TC) including both biogenic sources and anthropogenic emissions, was also monitored in real time (Rigler et al., 2020). The total organic carbon mass concentration (OC) is estimated by subtracting eBC from TC. Meteorological data and air pollution data (PM_{10} and $PM_{2.5}$) close to the observation sites in Fig. 1 were obtained from the weather station at MeteoSwiss Payerne (https://opendatadocs.meteoswiss.ch/a-data-groundbased/a1-automatic-weather-stations). The difference between PM_{10} and $PM_{2.5}$ was calculated and termed ΔPM, indicating coarse-sized dust particles which have sizes generally larger than 2.5 μm (Gao et al., 2024).

https://doi.org/10.5194/egusphere-2026-2699
Preprint. Discussion started: 29 May 2026

2.4 Remote sensing measurements

During the PERICLES campaign, lidar measurements were performed using a UV Fluorescence-Mie lidar to obtain the vertical profile of the aerosol backscatter coefficients at 355 nm ($b_{aer@355}$) and at 470 nm ($b_{aer@470}$). The lidar system is based on a pulsed Nd:YAG laser emitting pulses at 355 nm with energy of 130 mJ at 10 Hz repetition frequency. A 150 mm diameter telescope (focal length f=1125 mm) was used to collect the backscattered lidar signals. A set of dichroic mirrors with high reflectivity (>99%) at 355 nm followed by a Pellin-Broca prism ensure the emission of the laser beam only at 355 nm. The backscattered lidar signals at 355 nm and 470 nm were spectrally separated using high reflective dichroic beamsplitters. A spectrally narrow interference filter was used (FWHM = 0.5 nm) to detect the 355 nm lidar signals, while the fluorescence spectrum was optically filtered using a long-pass passband filter (cut-on at 400 nm), coupled with a 420–520 nm bandpass interference filter, centred at 470 nm, similar to the one used by Veselovskii et al. (2020). The acquired elastic lidar signals at 355 nm were processed using the automated Single Calculus Chain tool detailed in D'amico et al. (2016) and Mattis et al. (2016), to obtain the vertical profiles of the aerosol backscatter coefficient. In this paper the fluorescence lidar signals are utilized only in their range- and background-correction form. The lidar signals were averaged over a 5-minute period and only collected during nighttime to avoid interference from daytime solar radiation.

2.5 Air mass backward trajectories

The 7-day back trajectories for air-masses arriving at the sampling site were calculated by running the HYbrid SingleParticle Lagrangian Integrated Trajectory (HYSPLIT) model (Draxler and Hess, 1998; Stein et al., 2015). For each aerosol sample in Table S1, the start time for back trajectories was at the full hour closest to the sampling time. The model was launched every 6 h backward the start time. Meteorological data from the Global Data Assimilation System (GDAS, 1°×1° resolution) were imported. The source height was set at two height levels of 500 and 1000 m above the ground level, to avoid the influence from the orographic terrain. Additionally, the fire map data in the past 7 days was downloaded at the Fire Information for Resource Management System from the US National Aeronautics and Space Administration (NASA, https://firms2.modaps.eosdis.nasa.gov/map/#d:24hrs;@0.0,0.0,3.0z, last access: April 21, 2026) and used to depict the calculated air-mass back trajectories.

2.6 Aerosol particle visualization

An optical microscope (Olympus BX41) was used to collect images from Hirst samples. Three samples (Fig. 2b) on 20 June, 21 June and 22 June 2023 during the dust event period defined in Fig. 2d were analysed to provide visual evidence for the presence of dust and biological particles. Images were obtained at magnifications of x20, x40 and x60 by connecting a DSLR (Canon EOS 60D) to the microscope.

https://doi.org/10.5194/egusphere-2026-2699
Preprint. Discussion started: 29 May 2026

3 Results

PERICLES campaign is described in detail in a companion study (Gidarakou et al., 2026). We combined the in-situ, remote sensing and simulation results to identify INP sources, quantified the abundance of INPs of biological origin and linked them to different PBAP types and pollen. We also investigated the relative importance of transported mineral dust and local PBAPs. The effects of precipitation on INP abundance were examined through different case studies. Finally, we demonstrated that new INP parameterizations, which incorporate fluorescent properties to account for PBAPs and dust particles, outperform existing INP parameterizations (Tobo et al., 2013; Demott et al., 2010), with validation against datasets from other field campaigns in different regions.

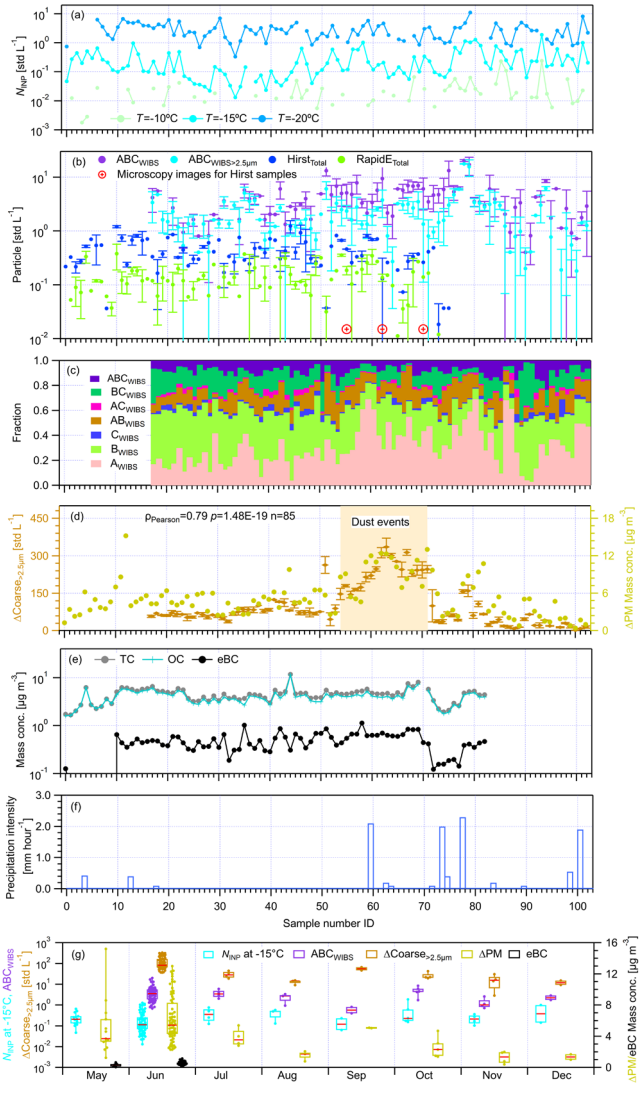

Figure 2. Overview of N_{INP} at three fixed temperatures and different aerosol properties for all IN samples. Detailed information on samples as a function of sample ID numbers is provided in the Supplement. (a) INP number concentration (N_{INP}) at −10, −15 and

https://doi.org/10.5194/egusphere-2026-2699
Preprint. Discussion started: 29 May 2026

−20°C. (b) The number concentration of ABC_{WIBS} and $ABC_{WIBS>2.5\mu m}$, $RapidE_{Total}$ and $Hirst_{Total}$ particles. Also, three Hirst samples with exemplary microscopy images are indicated. (c) The fraction pattern of different types of fluorescent particles classified by WIBS. Different types of particles are indicated in the legend. (d) The number concentration of $\Delta Coarse_{>2.5\mu m}$, i.e., the number concentration difference between $Total_{WIBS>2.5\mu m}$ and $ABC_{WIBS>2.5\mu m}$, on the left axis, and the mass concentration of ΔPM, i.e., the mass concentration difference between PM_{10} and $PM_{2.5}$, on the right axis. (e) The mass concentration of TC, eBC and OC (the difference between TC and eBC). (f) The precipitation intensity for the period of aerosol sampling. (g) Monthly box plots of number concentrations of N_{INP} at −15°C, ABC_{WIBS}, and $\Delta Coarse_{>2.5\mu m}$ (on the left axis), and mass concentrations of ΔPM and eBC (on the right axis). The red central mark indicates the median, and the bottom and top edges of the box indicate the 25th and 75th percentiles, respectively. All concentration values were corrected to equivalent atmospheric standard condition (i.e., per standard volume of sampled air, std). The error bars for bar plots represent 1 standard deviation of corresponding measurements. N_{INP} values are weighted averages of at least three measurements per sample, calculated following Wieder et al. (2022).

3.1 Overview of INPs and in-situ aerosol property observations

Figure 1a shows that INP concentration (N_{INP} at −10, −15 and −20°C) increases by roughly one order of magnitude for each 5°C decrease. At a given T, N_{INP} values across samples generally vary within one order of magnitude. Comparisons between N_{INP} observed in this study and previous studies in the region of Swiss Plateau and a global envelope by Petters and Wright (2015) are provided in Supplement Fig. S5 and discussed in Supplement Text S7. Here, we use fluorescent biological aerosol particles (FBAPs) that show fluorescence in all channels of the Wideband Integrated Bioaerosol Sensor (i.e., ABC_{WIBS}) to represent PBAP abundance, as did in other studies (Huffman et al., 2013; Cornwell et al., 2023). As shown in Fig. 1b, ABC_{WIBS} numbers are much larger than $Hirst_{Total}$ (including pollen, fungi and fungal spores measured by a Hirst) (Hirst, 1952) and $RapidE_{Total}$ (basically pollen measured by a Rapid-E) (Crouzy et al., 2016). The difference between ABC_{WIBS} (also $ABC_{WIBS>2.5\mu m}$, i.e., >2.5µm ABC_{WIBS} particles) and $RapidE_{Total}$ for different samples varies from a small range close to the measurement uncertainty (e.g., Sample ID=20 to 24 in Supplement Table S1) to more than two orders of magnitude (Sample ID=73 to 75 influenced by precipitation). This suggests the variability of local PBAP and pollen emission rates and their dependence on meteorological conditions. Additionally, we note that many intact pollen grains would be too large to be sampled by WIBS. This is supported by exemplary microscopy images for Hirst samples showing the presence of different biological particles, including pollen, spores and plant debris (>30µm, Supplement Figs. S6 to S8). The larger $Hirst_{Total}$ compared to $RapidE_{Total}$ may be because Hirst detects 48 types (Supplement S6) of pollen which is more than Rapid-E (11 types, Supplement S5). The Hirst sampler is reported to overestimate particle concentrations due to a flow rate bias, where the actual flow exceeds the calibrated value (Oteros et al., 2016). Figure 1c shows that a small fraction of (mostly >0.05) ABC_{WIBS} particles persistently exists for all samples. The fractions of A_{WIBS} and B_{WIBS} particles (detected only by the first or second WIBS channel) show larger variance than those of other particle types, which is likely due to nonbiological particle interference (Perring et al., 2015).

The difference between $ABC_{WIBS>2.5\mu m}$ and $Total_{WIBS>2.5\mu m}$ (i.e., total particles between 2.5 and 30 µm detected by WIBS) is calculated as $\Delta Coarse_{>2.5\mu m}$ to represent the upper number concentration estimation of coarse dust (Gao et al., 2024) including large FBAPs (Fig. 1d). Results in Supplement Fig. S6 to S8 support that $\Delta Coarse_{>2.5\mu m}$ may include both dust and FBAPs. To exclude some coarse FBAPs, the difference between $Fluo_{WIBS>2.5\mu m}$ and $Total_{WIBS>2.5\mu m}$ is calculated as $\Delta Coarse_{>2.5\mu m,nonFluo}$ (more details in Fig. S9 and Text S9 in Supplement) to represent the lower limit of dust particles. In

https://doi.org/10.5194/egusphere-2026-2699
Preprint. Discussion started: 29 May 2026

addition, ΔPM (i.e., the mass concentration difference between PM_{10} and $PM_{2.5}$) is used to indicate the abundance of dust in terms of particle mass. The strong and significant linear correlation between ΔPM and $\Delta Coarse_{>2.5\mu m}$ ($\rho_{Pearson}$=0.79 and p =1.48×10^{-19}) suggests that ΔPM can serve as a proxy for large dust particle abundance when $\Delta Coarse_{>2.5\mu m}$ is unavailable. Figure 1d shows that 19 samples (Sample ID between 54 and 72 with a shading) during the campaign are likely influenced by an intense dust event, supported by their relatively larger $\Delta Coarse_{>2.5\mu m}$ (>~150 std L^{-1}) and ΔPM values. A previous study (Gao et al., 2024) reported the presence of Saharan dust event when $\Delta Coarse_{>2.5\mu m}$ is larger than ~100 std L^{-1}. Air-mass back trajectory results and exemplary microscopy images for Hirst samples also support the identification of the above dust period.

Figure 1e provides the mass concentrations of total carbon (TC), organic carbon (OC) and elemental black carbon (eBC; used as a tracer for biomass burning aerosols), which vary about one order of magnitude. Figure 1f shows precipitation levels during each sample collection, which is important because precipitation may promote the release of FBAPs (Fig. 1b) but also remove aerosol particles (Fig. 1d and e) through wet scavenging. More results about the precipitation effects on aerosol properties and INP abundance are provided in Figs. S10 and S11 and the details are discussed in Supplement Text S10). In addition, Fig. 1g shows that monthly variability of N_{INP} at −15°C is more closely driven by ABC_{WIBS} changes, compared to $\Delta Coarse_{>2.5\mu m}$, ΔPM and eBC. This qualitatively suggests PBAPs may be more important drivers for INP variabilities than biomass burning aerosols and coarse-sized dust particles. Similar to Schneider et al. (2021), N_{INP} values in Fig. 1g were higher in summer and lower during the winter season. We note that 80% of samples in Fig. 1g were collected during the summer (Supplement Table S1), which may bias the statistical analysis of seasonal patterns. Therefore, we do not pursue further in-depth discussion of INP seasonality.

https://doi.org/10.5194/egusphere-2026-2699
Preprint. Discussion started: 29 May 2026

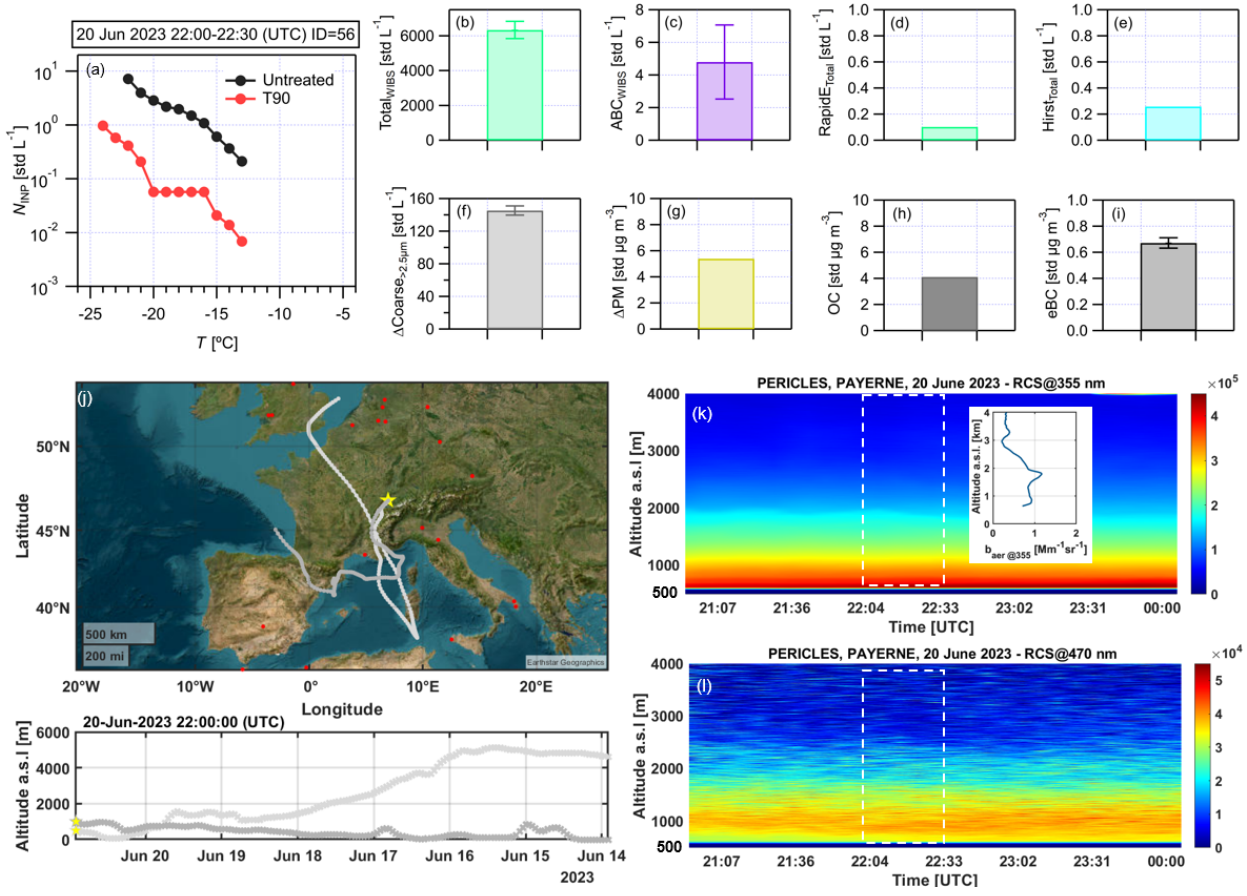

285 **Figure 3. Aerosol properties from in situ, modelling and remote sensing measurements for an INP sample (ID=56) collected on 20 June 2023, between 22:00 and 22:30 (UTC). (a) The INP number concentrations (N_{INP}) of untreated and 90°C heated (T90) samples. (b) $Total_{WIBS}$ particle number concentration. (c) ABC_{WIBS} particle number concentration. (d) $RapidE_{Total}$ particle number concentration. (e) $Hirst_{Total}$ particle number concentration. (f) $\Delta Coarse_{>2.5\mu m}$ particle number concentration. (g) ΔPM mass concentration. (h) OC mass concentration. (i) eBC mass concentration. (j) Air-mass atmospheric trajectories at 500 and 1000 m** 290 **above the ground level (a.g.l.) acquired from HYbrid Single–Particle Lagrangian Integrated Trajectory (HYSPLIT). The red dots indicate fire spots in the last 7 days. (k) Spatio-temporal evolution of the aerosol range-corrected lidar signals at 355 nm (RCS@355nm, in arbitrary units), with inset the averaged vertical profile of the aerosol backscatter coefficient at 355 nm ($b_{aer@355}$) for the period of INP sampling (time window indicated by the white dashed square). (l) Spatio-temporal evolution of the range-corrected aerosol fluorescent lidar signal centred at 470 nm (RCS@470nm, in arbitrary units). The colour bar in panel (k) and (l)** 295 **indicates the maximum normalized signal intensities. The error bars for bar plots represent 1 standard deviation of corresponding measurements. N_{INP} values are weighted averages of at least three measurements per sample, calculated following Wieder et al. (2022).**

3.2 INP source apportionment using a synergy of aerosol property characterization results: A case study

By combining air-mass back trajectory analysis with in-situ and lidar remote sensing measurements for each sampling 300 period, we identify aerosol sources using their distinct properties. Figure 3a shows that heating treatment at 90°C leads to significant decreases in N_{INP} compared to the untreated sample (more case studies in Supplement Figs. S12 to S19). This indicates important contributions from PBAPs to INPs (Murray et al., 2012; Kanji et al., 2017). The presence of FBAPs (i.e.,

https://doi.org/10.5194/egusphere-2026-2699
Preprint. Discussion started: 29 May 2026

ABC$_{WIBS}$, ~5.0 std L^{-1} in Fig. 3c) and pollen particles (represented by RapidE$_{Total}$ and Hirst$_{Total}$ in Fig. 3d and e respectively, ~0.1–0.3 std L^{-1}) supports the availability of PBAP sources for INPs. The remaining INPs in the corresponding T90 sample (heated at 90°C before IN experiments) for T>–15°C (<0.03 std L^{-1}) may originate from trace mineral/soil dust or heat-resistant organics (Hill et al., 2016; Conen et al., 2022). Notably, constant N_{INP} levels between –16 and –20°C for the T90 sample (Fig. 3a) suggests complete deactivation of INP subgroups found in the untreated sample. For INPs observed at T<–20°C, coarse-sized soil and mineral dust particles (ΔCoarse$_{>2.5\mu m}$, ΔPM in Fig. 3f and g respectively) may be relevant. Heating at 90°C leads to a reduction of N_{INP} for T<–20°C by approximately one order of magnitude (Fig. 3a), which is a relatively lower reduction than observed for warmer temperatures. The reduction may result from deactivation of soil dust containing heat-labile biological material (O'sullivan et al., 2013). In addition, the corresponding OC level for the INP sample (Fig. 3h) may be from organic-containing aerosol particles, e.g., organic particles, PBAPs and particles with organic coatings. The presence of eBC (Fig. 3i) indicates the influence of biomass burning aerosols, partially supported by the air-mass back trajectories in Fig. 3j passing by a few fire spots. The spatio-temporal evolution of range-corrected signals from total and fluorescent aerosol particles, measured by the lidar at 355 nm and 470 nm channels (Fig. 3k and l, respectively), clearly shows that aerosol particles are concentrated in distinct layers between heights of 500m, 1000m and 1500m a.s.l. Notably, each layer shows homogeneous mixing of particles, with decreasing aerosol abundance with increasing altitude. Thus, ground-level INP samples mainly reflect local sources, though long-range transported air-masses (Fig. 3j) can mix with lower boundary layer aerosols (~1000 m, in Fig. 3k and l) before reaching the surface.

In general, FBAPs (including some pollen particles), some dust particles represented by coarse-sized particles and eBC containing particles (likely from transported biomass burning aerosols, vehicle emissions from nearby highway, and fuel combustion from nearby household), were observed in the vicinity of the sampling site. These particles were the source of potential INPs. The spatio-temporal evolution of the aerosols observed by the bio-lidar suggests the major role of local particle emissions in the boundary layer as INP sources (more results in Figs. S12 to S19 in Supplement S11).

https://doi.org/10.5194/egusphere-2026-2699
Preprint. Discussion started: 29 May 2026

3.3 Dependence of INPs on different types of particles

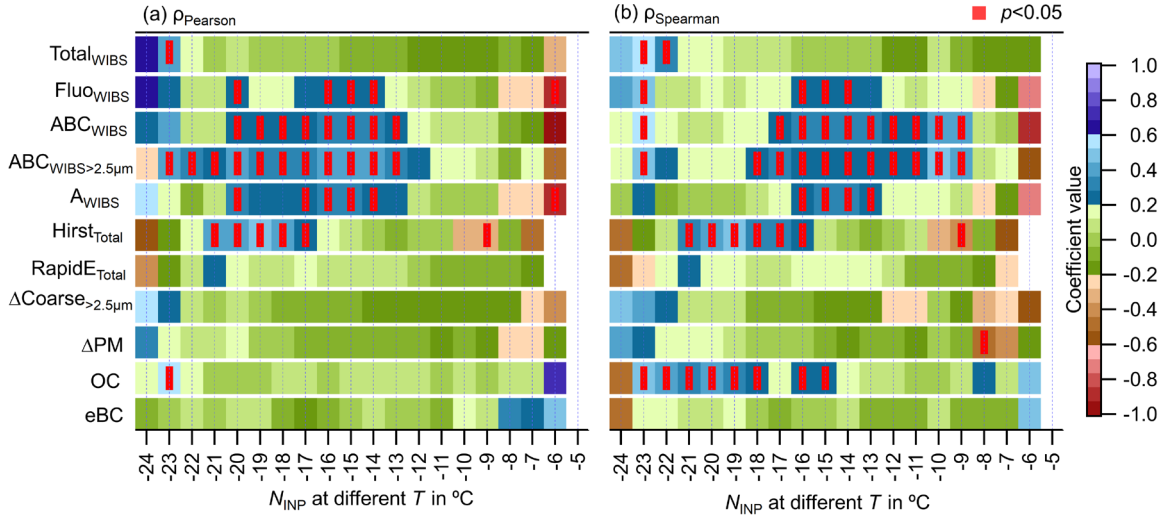

Figure 4. The correlation coefficients between N_{INP} at a fixed T (on the x-axis) for untreated samples and different aerosol properties. The presented aerosol properties include $Total_{WIBS}$, $Fluo_{WIBS}$, ABC_{WIBS}, $ABC_{WIBS>2.5\mu m}$, A_{WIBS}, $Hirst_{Total}$, $RapidE_{Total}$, $\Delta Coarse_{>2.5\mu m}$, ΔPM, OC and eBC. (a) Pearson coefficient ($\rho_{Pearson}$). (b) Spearman coefficient ($\rho_{Spearman}$). The coefficient values scale to the colour bar. A red rectangle indicates a significant correlation with a p value smaller than 0.05.

Figure 4 presents the heat map for Pearson and Spearman coefficients ($\rho_{Pearson}$ and $\rho_{Spearman}$, respectively) between N_{INP} at different fixed temperatures and aerosol properties that help characterize INP sources. Detailed data for each block in the heat map is provided in Figs. S20 to S29 in Supplement S12. $Total_{WIBS}$ (i.e., total particles between 0.5 and 30 μm detected by WIBS) generally shows a weak correlation with N_{INP} ($\rho_{Pearson}$ and $\rho_{Spearman}$ <0.2), reflecting the scarcity of INPs relative to the total abundance of even coarse particles for warm MPCs (Demott et al., 2010; Gao et al., 2024). Only for T=−23°C, does the $\rho_{Pearson}$ show a medium correlation (~0.41) and become significant (Fig. 4a). Similarly, $\rho_{Spearman}$ values between $Total_{WIBS}$ and N_{INP} only become significant for T=−22 and −23°C (Fig. 4b). The slightly negative correlations for T>−15°C, but positive correlations for lower Ts, suggest that $Total_{WIBS}$ cannot represent INP abundance at warm Ts, where mainly PBAPs may act as INPs, because PBAPs constitute only a minor fraction of total particles (e.g., FBAPs represented by ABC_{WIBS} is <0.1 of $Total_{WIBS}$ in Fig. 2c). This highlights the need to monitor PBAPs for predicting INPs at warm Ts. In addition, $Fluo_{WIBS}$ and N_{INP} are weakly (both $\rho_{Pearson}$ and $\rho_{Spearman}$ <0.4) but significantly correlated for T around −15°C; the insignificant correlation of $Fluo_{WIBS}$ for warmer and colder Ts means that $Fluo_{WIBS}$ is not directly related to INPs at these Ts. However, ABC_{WIBS} particles, a subclass of FBAPs, show significant correlations ($\rho_{Pearson}$ and $\rho_{Spearman}$ ~0.4) with INPs for −19°C< T <−9°C. Coarse-sized FBAPs represented by $ABC_{WIBS>2.5\mu m}$ show similar results for −22°C< T <−9°C. In a companion study (not published), we presented even stronger correlations (larger $\rho_{Pearson}$ and $\rho_{Spearman}$ by ~0.2) between ABC_{WIBS} (also $ABC_{WIBS>2.5\mu m}$) and deactivated N_{INP} (after heating) which more closely represent INPs of biological origin than total INPs used in Fig. 4. Altogether, our results suggest that fluorescence characteristics are good indicators of

https://doi.org/10.5194/egusphere-2026-2699
Preprint. Discussion started: 29 May 2026

immersion-mode INPs in warm (T>−20°C) MPCs. Furthermore, it suggests that FBAPs, in particular coarse-sized FBAPs ($ABC_{WIBS>2.5\mu m}$), contribute to the observed INPs, which is consistent with Cornwell et al. (2023). This is because the largest particles that fluoresce are associated with coarse-sized PBAPs, like pollen or pollen fragments, some of which are known to be effective INPs (Augustin et al., 2013). Also, it is notable that $ABC_{WIBS>2.5\mu m}$ shows significant correlations for INPs tested at T<−18°C at which ABC_{WIBS} shows insignificant correlations. This may indicate the fact that large pollen particles, part of $ABC_{WIBS>2.5\mu m}$, only act as INPs for T around −20°C, and not for warmer temperatures (Augustin et al., 2013). Moreover, extra results in the Supplement Figs. S22 and S23 suggest that both ABC_{WIBS} and $ABC_{WIBS>2.5\mu m}$ particles can be used to estimate 99% N_{INP} values at −20°C within one order of magnitude. In addition, A_{WIBS} particles, representatives for bacteria and fungal spores (Tang et al., 2022), exhibit significant correlations ($\rho_{Pearson}$ and $\rho_{Spearman}$ ~0.4) with N_{INP} between −13°C and −17°C. Figure 4 further shows that pollen particles (likely also fungi and fungal spores, see Supplement Figs. S6 to S8) represented by $Hirst_{Total}$ are significantly correlated ($\rho_{Pearson}$ and $\rho_{Spearman}$ ~0.5) with INPs between −16°C and −21°C, affirming a pollen contribution to INPs, consistent with the literature (O'sullivan et al., 2018; Murray et al., 2022; Augustin et al., 2013). In contrast, $RapidE_{Total}$ does not show significant correlations with N_{INP} at any T, likely because of the more limited pollen detection ability of Rapid-E (11 taxa) than Hirst (48 taxa) and suggesting pollen IN ability is species dependent.

It is reported that coarse-sized particles, particularly dust particles, are generally more active INPs than other small-sized particles (Kanji et al., 2017; Demott et al., 2010). However, Fig. 4 shows that both $\Delta Coarse_{>2.5\mu m}$ and ΔPM are not significantly correlated with the observed INPs at any T, suggesting here they are inappropriate predictors for INPs. This can be statistically true when their contribution to INPs is insignificant. Additionally, this may be owing to the inefficient IN of these particles (e.g., soil dust in Argentina (Steinke et al., 2016) and long-range transported Saharan dust (Patnaude et al., 2025) after intensive atmospheric aging) at warm MPC temperatures. Therefore, particle types, in addition to size, must be differentiated to better examine INP sources.

Figure 4a shows insignificant correlations between OC and INPs whereas Fig. 4b shows significant correlations ($\rho_{Spearman}$ ~0.4) between the two for −23°C< T <−15°C. This may suggest a non-linear dependence of N_{INP} on OC abundance sourced from active PBAPs. Additionally, insignificant correlations between eBC and INPs presented in Fig. 4 may suggest black carbon particles, e.g., in biomass burning aerosols, do not act as immersion-mode INPs. This is in agreement with the literature reporting that eBC particles only nucleate ice at T <−38°C (Kanji et al., 2020). In summary, Fig. 4 reveals that coarse-sized PBAPs may contribute significantly to the observed INPs and may be more important than biomass burning aerosols and coarse-sized dust particles. At warm Ts, only certain PBAPs are active INPs but not all $Fluo_{WIBS}$ which contain interfering particles, like eBC, while dust particles become increasingly important with decreasing T.

https://doi.org/10.5194/egusphere-2026-2699
Preprint. Discussion started: 29 May 2026

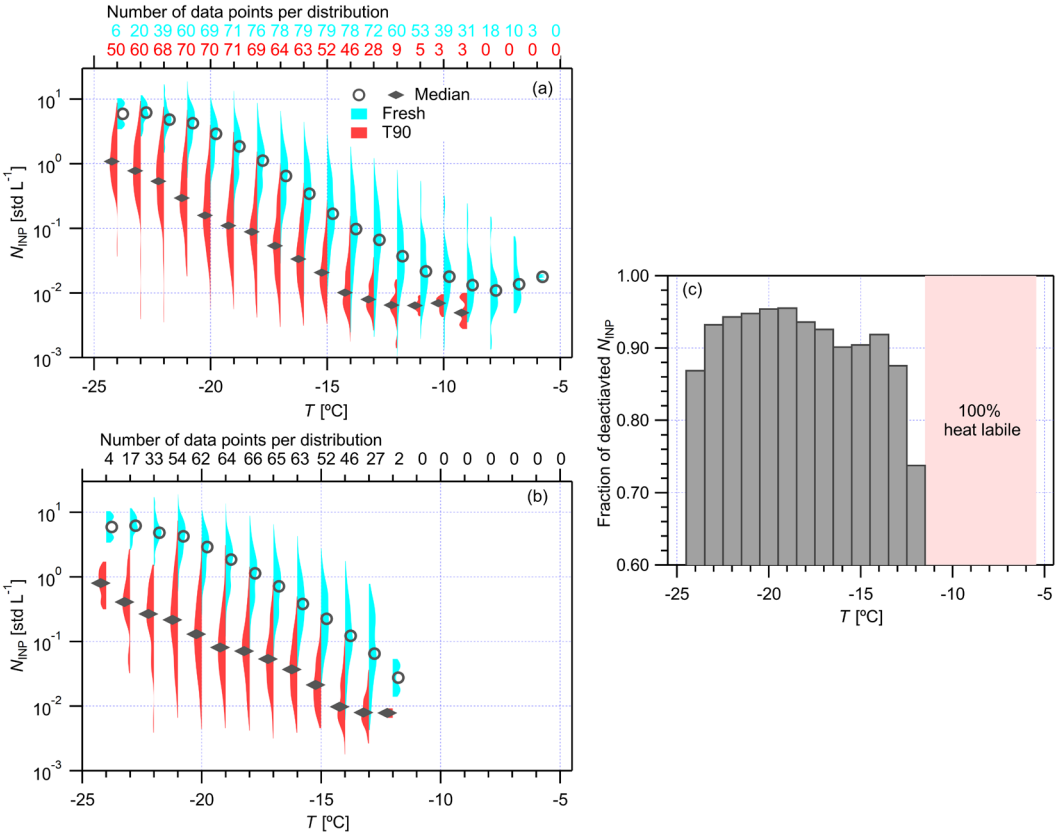

Figure 5. Effects of heating on INP abundance. (a) Violin plots for the comparison of N_{INP} of samples before ("untreated") and after ("T90") heating treatment at 90°C (n=79). The median value for each distribution is shown by a grey circle (untreated) or diamond (T90). The number of data points at each temperature is provided at the top of the panel (in light blue and red for untreated and T90 samples, respectively). (b) N_{INP} violin plots of all samples (n=66) whose N_{INP} values of both untreated and T90 samples at the same T are available. (c) Fraction of deactivated N_{INP} (dN_{INP}) at different temperatures represented by the ratio of the median of dN_{INP} of T90 samples to the median N_{INP} of untreated samples, where the dN_{INP} of T90 samples equals to the difference between the median N_{INP} of T90 and untreated samples presented in panel (b).

3.4 Heat-labile particles as dominant INP sources

Heating treatment was widely used to test the contribution of heat-labile particles to INPs, such as proteins or biological macromolecules from PBAPs (O'sullivan et al., 2018; Li et al., 2023). We heated 79 of 103 total samples at 90°C, termed T90 (Supplement Table S1). Such a large data set allows us to quantify the contribution of heat-labile INPs for the whole campaign. Figure 5a compares the N_{INP} spectra of T90 samples to corresponding untreated samples. Figure 5b compares untreated to T90 samples only when both have detectable INPs at the same T. Figure 5c further shows the deactivated INP fractions of T90 samples using median values presented in Fig. 5b.

For $T \geq -8$°C, INPs of 18 T90 samples are completely degraded or below the detection limit (Fig. 5a), clearly suggesting the contribution of heat-labile bacteria (Lukas et al., 2022; Stopelli et al., 2017), fungi or fungal spores (Fröhlich-Nowoisky et

https://doi.org/10.5194/egusphere-2026-2699
Preprint. Discussion started: 29 May 2026

al., 2015), and soil dust particles carrying active ice nucleating proteins (O'sullivan et al., 2013) to the observed INPs. Between −9°C and −12°C, only 9 of 79 T90 samples retain detectable INPs (Fig. 5a) despite 60 of 79 untreated samples contain INPs at −12 °C (Fig. 5a), still showing that many heat-treated samples fall below the instrument detection limit. The deactivated INP (dN_{INP}) fraction at −12°C is ~0.74 (Fig. 5c), based on the only two T90 samples showing detectable INPs (Fig. 5b). Since most T90 samples fall below the INP detection limit, the true dN_{INP} fraction is likely >0.74, indicating a strong deactivation effect of heating on INPs associated with heat-labile biogenic material (Li et al., 2023; O'sullivan et al., 2018). For T<−12°C, the dN_{INP} fraction of T90 samples are consistently more than 85% (Fig. 5c). In summary, Figure 5 quantifies the dominant contribution of heat-labile, very likely biological INPs, accounting for >~85%. This finding is consistent with the other field studies which qualitatively reported the primary role of PBAPs for INPs observed in vegetated regions (Tobo et al., 2013; Pereira Freitas et al., 2023; Cornwell et al., 2023; Schneider et al., 2021). Likely, the small fraction (<~15%) of remaining INPs for T≤−12°C can be attributable to heat-resistant organic or dust particles (Hill et al., 2016; Suski et al., 2018).

3.5 The limit role of dust event in the observed INP abundance

To further access the role of dust in the observed INPs, we first examine air-mass back trajectories arriving at a height of 500 m and 1000 m above the ground level (a.g.l.) for INP samples collected during and outside the dust-event period (Fig. 2d) in Fig. 6 to identify dust plumes, and then quantify dust contribution to immersion-mode INPs (Fig. 7).

Figure 6a (500 m a.g.l.) and b (1000 m a.g.l.) show the back trajectories of air-masses for samples during the dust period. More than half (10 of 19) of air-mass back trajectories originate from the Saharan desert, which explains the higher (approximately double those outside the dust period) concentration of $Total_{WIBS}$, $\Delta Coarse_{>2.5\mu m}$ and ΔPM particles observed in-situ (Fig. 2, and Fig. 7a, b and c). Remote sensing results also confirm that air-masses below 500 m a.g.l. are generally well-mixed (Fig. 3k, and Fig. S18k and Fig. S19k in Supplement S11) such that they can influence INPs observed at ground level. Furthermore, the prevalence of coarse-sized mineral dust particles in the microscopy images for Hirst samples (Figs. S6 to S8 in Supplement S8, relevant for samples with ID=55, 62, 67 and 70 during dust period) provides visual evidence on the influence of dust. In contrast, air-mass back trajectories for the 16 samples collected outside the dust period (Fig. 6c and d) show no influence from Saharan dust, instead indicating continental or marine air-masses, consistent with the low $\Delta Coarse_{>2.5\mu m}$ number concentration (Fig. 2d)) characteristics of non-dust aerosols (Gao et al., 2024).

https://doi.org/10.5194/egusphere-2026-2699
Preprint. Discussion started: 29 May 2026

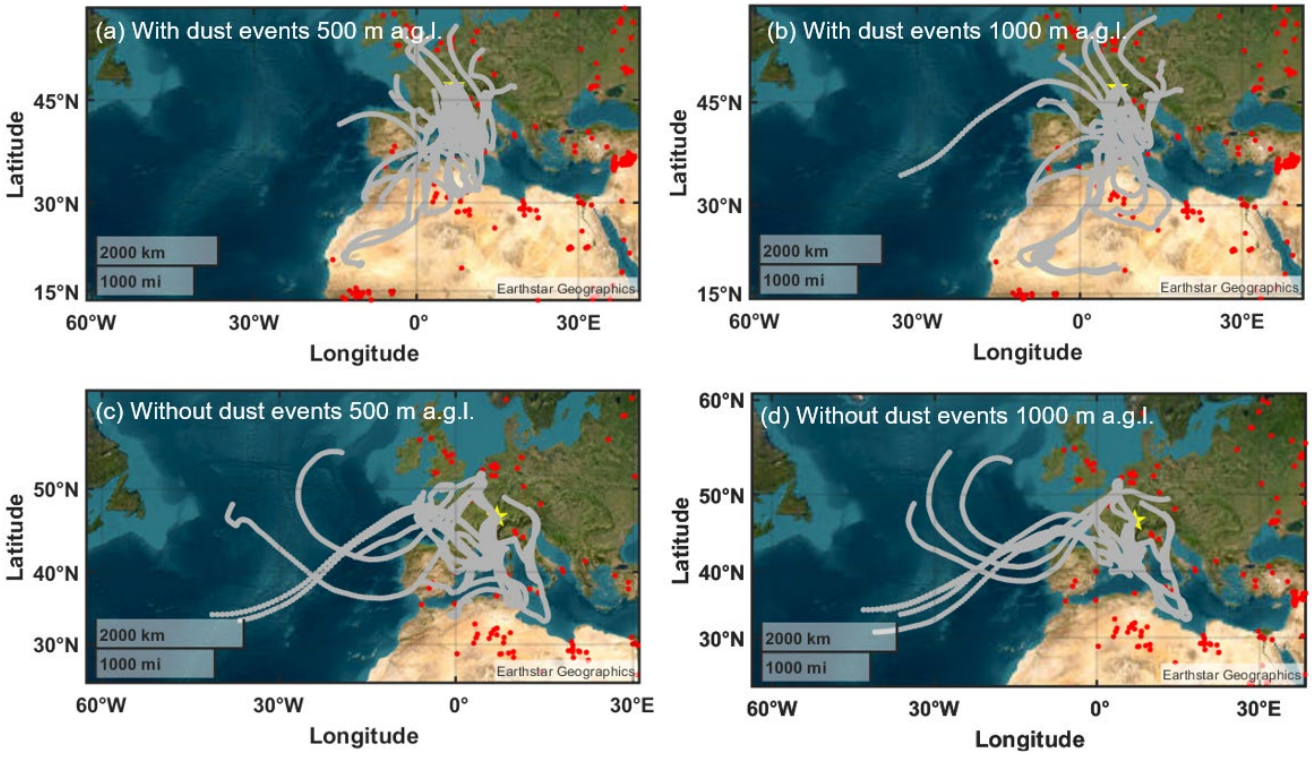

Figure 6. Air-mass back trajectory (past 7 days) groups for INP samples with and without the influence of dust event. Samples with dust event influence correspond to samples with an ID from 54 to 72 (n=19, see Fig. 1D and Supplementary Materials Table S1). Samples (16) without dust event influence correspond to samples with an ID from 46 to 53 (n=8, before dust period) and 73 to 80 (n=8, after dust period), collected through five consecutive days from 19 June to 23 June 2023. Panel (a) and (b) show trajectories arriving at 500 m and 1000 m a.g.l., respectively, for the samples during dust events. Panel (c) and (d) shows trajectories arriving at 500 m and 1000 m a.g.l., respectively, for samples outside dust event period. The red dots indicate fire spots in the past 7 days obtained from the Fire Information for Resource Management System from the US National Aeronautics and Space Administration (https://firms.modaps.eosdis.nasa.gov/map).

https://doi.org/10.5194/egusphere-2026-2699
Preprint. Discussion started: 29 May 2026

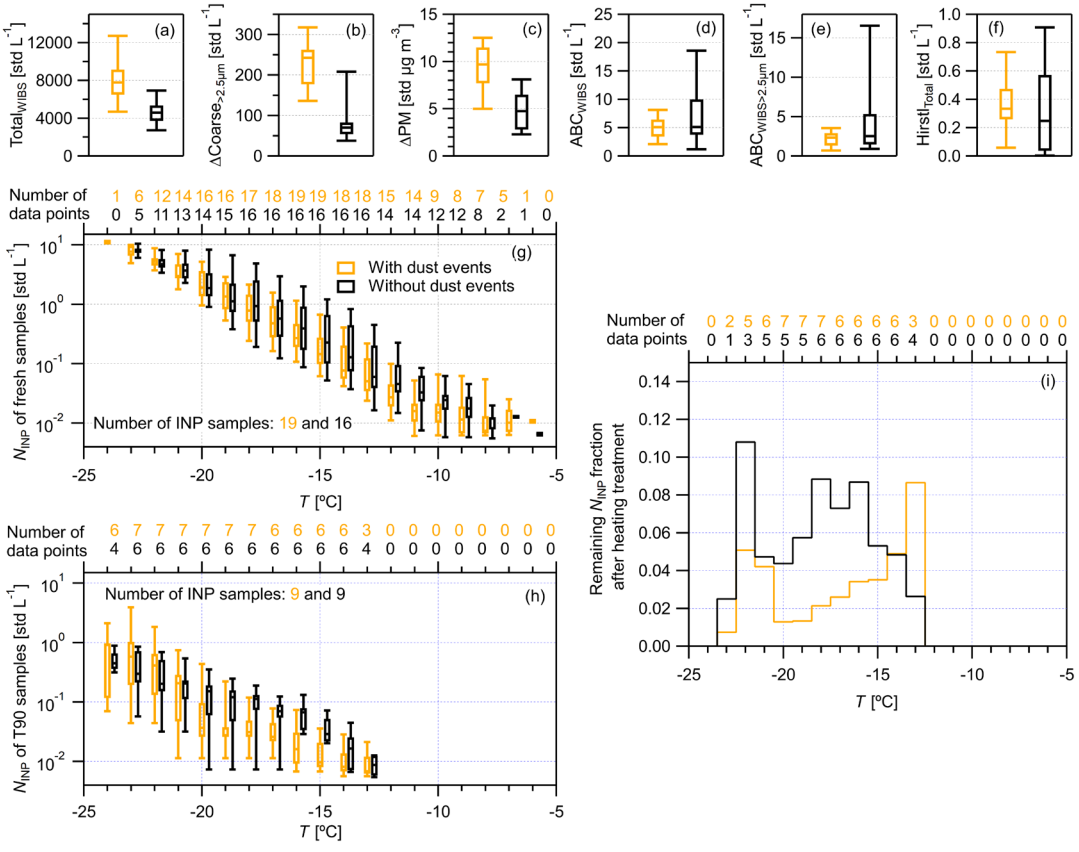

Figure 7. Contribution of dust particles to the observed INPs during and outside dust events. Samples with dust event influence are with ID 54 to 72 (n=19, see Fig. 2d and Supplement Table S1). Samples (16) without dust event influence are with ID 46 to 53 (n=8, before dust period) and 73 to 80 (n=8, after dust period). Panel (a) to (f) present box plots of different aerosol properties, including $Total_{WIBS}$ (a), $\Delta Coarse_{>2.5\mu m}$ (b), ΔPM (c), ABC_{WIBS} (d), $ABC_{WIBS>2.5\mu m}$ (e), $Hirst_{Total}$ (f), for the three sample groups. Panel (g) and (h) shows the N_{INP} values as a function of T for untreated and T90 samples, respectively. Panel (i) presents the fraction of remaining N_{INP} of T90 samples for both groups. The fraction values are calculated using the median N_{INP} values of untreated and corresponding T90 samples when N_{INP} of both samples are available/detectable. Those samples were collected on five consecutive days from 19 June to 23 June 2023. Each sample group is represented by a colour as indicated in Panel (g) legend.

Our results show that the absence of dust events is associated with more variability in FBAPs (Fig. 7d and e for ABC_{WIBS} and $ABC_{WIBS>2.5\mu m}$, respectively) and pollen (Fig. 7f for $Hirst_{Total}$), sometimes showing much more abundant PBAPs (by a factor of ~2). N_{INP} values of untreated samples (e.g., median of 0.23 std L^{-1} at −15°C) without dust influence for −18< T <−6°C are overall even larger than samples with dust influence (e.g., median of 0.14 std L^{-1} at −15°C, Fig. 7g). Together, this suggests that enriched coarse-sized dust particles make insignificant contribution to the observed immersion-mode INPs. In contrast, this highlights the importance of IN-active biological particles for cloud ice formation at warm Ts. For T<−18°C, the N_{INP} values of dust influenced samples are slightly higher than those of samples outside dust period, e.g., median N_{INP} = 1.36 std L^{-1} of the former and 1.12 std L^{-1} of the latter at −19°C (Fig. 7g). This suggests the small contribution of dust

https://doi.org/10.5194/egusphere-2026-2699
Preprint. Discussion started: 29 May 2026

particles to INPs at T<−18°C, which is consistent to the activation of dust particle lower than −15°C generally reported in the literature (Murray et al., 2012).

Figure 6h shows that the INP concentration of 2 (3) T90 samples from the dust (non-dust) group are below the measurement detection limit, which suggests the dominance of heat-labile INPs in those samples (Hill et al., 2016; Conen et al., 2022). For T>−20°C, the N_{INP} (remained INPs) of T90 samples from non-dust group is overall higher than those of the dust group at the same T, particularly for −19< T <−15°C. This suggests the nonnegligible role of heat-resistant INPs for warm temperatures, following heat-labile PBAPs. Differently, previous field observations at Jungfraujoch (3800m a.s.l.) on the Swiss Plateau (Brunner et al., 2021; Lacher et al., 2021) and Mt. Helmos (2314m a.s.l.) in the eastern Mediterranean (Gao et al., 2024) reported more pronounced INP enrichment during Saharan dust events. This is likely attributable to the relatively lower altitude of the observation site in this study (491 m a.s.l.), where transported dust particles undergo more intensive atmospheric aging within the planetary boundary layer (Fig. 3k), leading to somewhat reduced IN activity. In addition, for T≤−20°C, T90 samples during Saharan dust events preserve more INPs in comparison to the non-dust group (Fig. 7i). This suggests the enrichment of heat-resistant particles acting as INPs in the dust active regime because of the dust event, consistent with observations at Jungfraujoch (Brunner et al., 2021; Lacher et al., 2021) and Mt. Helmos (Gao et al., 2024).

Figure 7i compares the fraction of heat-resistant INPs in dust and non-dust influenced groups. Overall, heat-resistant INPs constitute <10% in both groups. It also shows that dust events only slightly enrich heat-resistant INPs for T≤−20°C but not for warm Ts. In other words, our results demonstrate that heat-labile FBAPs are the dominant source of INPs, irrespective of dust presence.

Table 1. Different parameterizations for predicting N_{INP} values observed in three field campaigns at a semi-rural site in Swiss Plateau (Payerne, Switzerland, this study), Mt. Helmos (Peloponnese, Greece) and Ny-Ålesund (Svalbard, Norway).

INP Parameterizations	Used aerosol property	Formulation
DeMott2010	$Total_{APS}$ (std cm^{-3})	$N_{INP} = a(-T)^b * Total_{APS}^{(-cT+d)}$ (a = 0.0000594, b = 3.33, c = 0.0264, d = 0.0033) ($Total_{APS}$ in std cm^{-3}; T in °C)
Adapted DeMott2010		$N_{INP} = a(-T)^b * Total_{APS}^{(-cT+d)}$ (a = 1.946E-12, b = 8.8976, c = −0.0095, d = 0.9973) ($Total_{APS}$ in std cm^{-3}; T in °C)
Tobo2013	$Fluo_{WIBS}$ (std cm^{-3})	$N_{INP} = Fluo_{WIBS}^{(-aT+b)} * \exp(-cT + d)$ (a = −0.108, b = 3.8, c = 0, d = 4.605) ($Fluo_{WIBS}^{@}$ in std cm^{-3}; T in °C)
Adapted Tobo2013		$N_{INP} = Fluo_{WIBS}^{(-aT+b)} * \exp(-cT + d)$ (a = 0.0108, b = 0.2759, c = 0.6332, d = −11.2925) ($Fluo_{WIBS}^{@}$ in std cm^{-3}; T in °C)
$WIBS_{Fluo}$		$N_{INP} = \exp(aT + b) * (Fluo_{WIBS}/1000)^{(cT+d)} * (WIBS_{ratio})^{(eT+f)}$ (a = −0.0080, b = −10.2353, c = −0.0552, d = −0.07910 e = 0.0720, f = 0.0066; T in °C)
$WIBS_{Total}$_1	$Total_{WIBS}$ (std L^{-1})	$N_{INP} = \exp(aT + b) * Total_{WIBS}^{(cT+d)} * (WIBS_{ratio} * e + f)$ (a = −0.5830, b = −24.9703, c = 0.0033, d = 1.0447, e = −1170.7188, f = 391.5464; T in °C)

https://doi.org/10.5194/egusphere-2026-2699
Preprint. Discussion started: 29 May 2026

$WIBS_{Total}\_2$	$N_{INP} = a(-T)^b * Total_{WIBS}{}^{(cT+d)} * (\frac{1}{WIBS_{ratio} * e + f})$ (a = $-5.88E-5$, b = -4.48, c = -0.0365, d = 0.0490, e = 36660, f = -21000; T in °C)

Note. *Adapted DeMott2010 uses the same formulation as that used in DeMott2010 but with a new suite of parameters. †Adapted Tobo2013 uses the same formulation as that used in Tobo2013 but with a new suite of parameters. ‡$WIBS_{ratio}$ is the ratio of $Fluo_{WIBS}$ to $NonFluo_{WIBS}$ (the difference between $Fluo_{WIBS}$ and $Total_{WIBS}$) particle concentration.

3.6 Parameterization of INPs sourced from PBAPs and dust particles

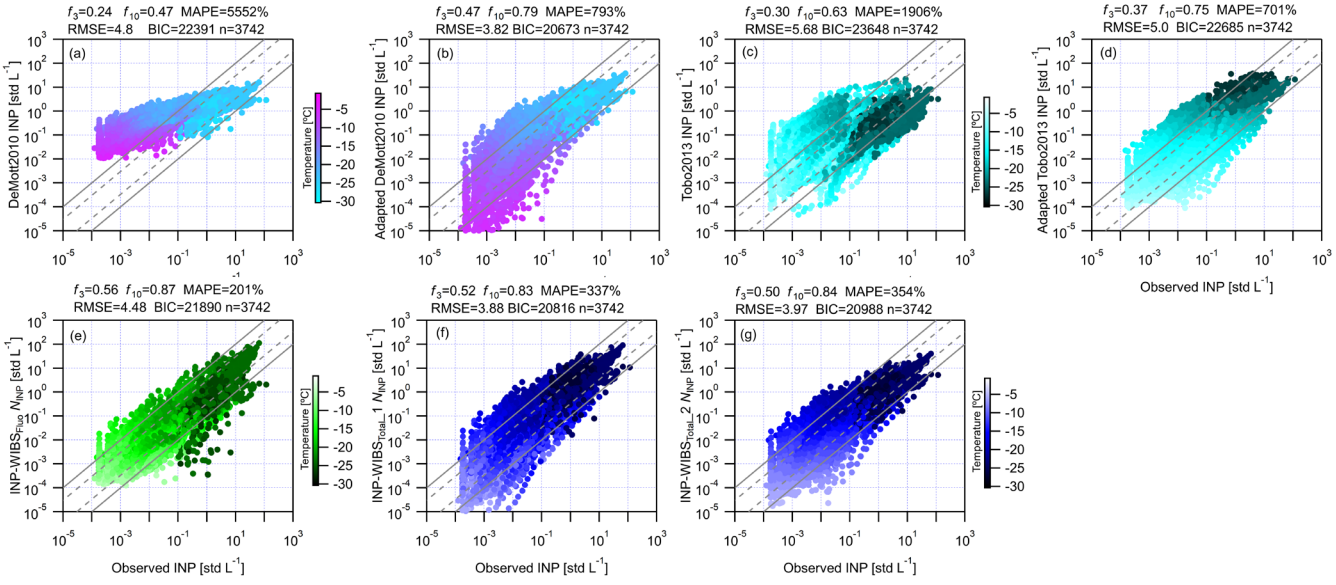

Figure 8. Comparisons of the performance of different parameterizations in Table 1. (a) DeMott2010. (b) Adapted DeMott2010 using a new set of parameters calculated by fitting the formula to the observed data. (c) Tobo2013. (d) Adapted Tobo2013 using a new set of parameters calculated by fitting the formula to the observed data. (e) $WIBS_{Fluo}$. (f) $WIBS_{Total}\_1$. (g) $WIBS_{Total}\_2$. The temperature condition for INP data is scaled to the color bar. Note that parameterizations using the same parameterization formula use the same color bar. The dashed lines confine the range for observed and predicted data points within a factor of 3. The fraction of observed and predicted data points within a factor of 3 (f_3) and 10 (f_{10}) is provided in each panel, respectively. MAPE stands for mean absolute percentage error. RMSE is the root-mean-square error used as a measure of the difference between observed and predicted data. BIC is a value calculated by applying the Bayesian information criteria to evaluate the goodness of parameterizations based on the same dataset (Schwarz, 1978). The *n* value shows the number of observed data points.

Here, we develop a universal INP parameterization (Gao et al., 2024) based on INP observations at different locations, including a semi-rural site on the Swiss Plateau (Payerne, Switzerland, this study), mountain top site at Mt. Helmos (Peloponnese, Greece) (Gao et al., 2024) and a remote site at Ny-Ålesund (Svalbard, Norway) (Li et al., 2023; Li et al., 2022). Varying INP sources, including particles from biological origin, local soil dust and long-range transported dust, were reported to be relevant INP sources for Mt. Helmos and Ny-Ålesund. Together with this study, the combined dataset of these three field campaigns (see Supplement Fig. S30) can serve as an inclusive statistical basis relevant for different types of INP sources, with PBAPs as distinguished contributors. Different INP formulations are listed in Table 1. The first

https://doi.org/10.5194/egusphere-2026-2699
Preprint. Discussion started: 29 May 2026

parametrization, termed INP-WIBS$_{Fluo}$, is as a function of Fluo$_{WIBS}$, the ratio of fluorescent (Fluo$_{WIBS}$) to nonfluorescent (NonFluo$_{WIBS}$) particles (WIBS$_{ratio}$) and T. The other two parameterizations ("INP-WIBS$_{Total}$_1" and "INP-WIBS$_{Total}$_2") use Total$_{WIBS}$, WIBS$_{ratio}$ and T but with different formula forms. WIBS$_{ratio}$ represents the partitioning of fluorescent particles and is demonstrated as a distinct indicator of different aerosol sources, including dust, continental aerosols and PBAPs (Gao et al., 2024).

The above three formulations are also evaluated against literature parameterizations. The first one is termed DeMott2010 using the total concentration of particles larger than 0.5 μm aerodynamic size (Demott et al., 2010). Here, we use Total$_{WIBS}$ (>0.5 μm optical size) for DeMott2010. DeMott2010 is based on field studies at different locations over a period of >10 years and widely used in models. The second one is called Tobo2013 which calculates N_{INP} as a function of T and the number concentration of total fluorescent particles >0.5 μm aerodynamic size (Tobo et al., 2013). Here, we use Fluo$_{WIBS}$ (>0.5 μm optical size) for Tobo2013. Both DeMott2010 and Tobo2013 are adapted by fitting the formula to the combined dataset to calculate a new set of parameters.

As shown in Fig. 8a, DeMott2010 predicts less than 50% data points within a factor of 10 (f_{10}=0.47) and approximately 25% data points within a factor of 3 (f_3=0.24) compared to the observed data. It predicts better for N_{INP} observed at T<−20°C, where mineral dust particles are more relevant INP source but not PBAPs relevant for warmer temperatures (Gao et al., 2024; Kanji et al., 2017). For N_{INP} observed at T>−10°C, values predicted by DeMott2010 exceed observations by more than a factor of 10. After adapting DeMott2010, its f_{10} (f_3) predictability improves to 0.79 (0.47), with gains primarily for INPs observed at warm temperatures (Fig. 8b), attributable to PBAP source (Gao et al., 2024; Murray et al., 2012). In addition, Tobo2013 (Fig. 8c) shows larger f_{10} (f_3) values by 0.16 (0.06) than DeMott2010. However, Tobo2013 shows a larger root-mean-square error (RMSE), indicating a larger spread range of the prediction. Also, the Bayesian information criteria (BIC) value calculated for Tobo2013 is larger than that of DeMott2010, suggesting a less satisfactory parameterization. Figure 8d shows that Adapted Tobo2013 improves f_{10} (f_3) performance to 0.75 (0.37), suggesting that particle fluorescence can enhance N_{INP} predictability. We further show that, by explicitly including fluorescent particles into the parameterization (i.e., their fraction in the aerosol source represented by WIBS$_{ratio}$) and their implicit higher INP efficiency, INP-WIBS$_{Fluo}$ can confine approximately 90% (>50%) of calculated and observed data points within a factor of 10 (or 3, in Fig. 8e). Higher WIBS$_{ratio}$ values indicate a larger fraction of fluorescent particles, likely more PBAPs with enhanced IN activity compared to dust. Therefore, incorporating WIBS$_{ratio}$ better captures particle IN ability, as potential INP abundance scales with total particle availability (Gao et al., 2024). In addition, INP-WIBS$_{Total}$_1 and INP-WIBS$_{Total}$_2 can predict approximately 85% (>50%) N_{INP} observations within a factor of 10 (3) (Fig. 8f and g). Compared to Adapted Tobo2013, our three parameterizations also show decreased BIC values. In addition, better performance of our parameterizations can be seen from comparisons of all parameterizations based on INPs observed for T≥−15°C (Fig. 9). Notably, INP-WIBS$_{Fluo}$ shows good predictability (f_{10}=0.53 and f_3=0.85) for INPs at T≥−15°C and outperforms the others by showing larger f_{10} (f_3) performance than DeMott2010, Adapted DeMott2010, Tobo2013, Adapted Tobo2013, WIBS$_{Total}$_1 and INP-WIBS$_{Total}$_2 by 0.6 (0.47), 0.11 (0.13), 0.24(0.2), 0.04 (0.1), 0.08 (0.13) and 0.04 (0.08), respectively. Results for INPs at warm Ts in Fig. 9 further highlight the

https://doi.org/10.5194/egusphere-2026-2699
Preprint. Discussion started: 29 May 2026

advantage of bioaerosol-aware INP parameterizations over existing ones. We also compare the application of INP-WIBS parameterizations across individual field campaigns (Supplement Fig. S31) and demonstrate that INP-WIBS$_{Fluo}$ is better suited for field sites with higher PBAP abundance. The better performance of INP-WIBS$_{Fluo}$ is likely because of its stronger focus on PBAPs, the main INP contributors. Therefore, our results demonstrate the superiority of using FBAPs and their indication on INP source apportioning to predict N_{INP} observations, and we propose INP-WIBS$_{Fluo}$ for modelling applications.

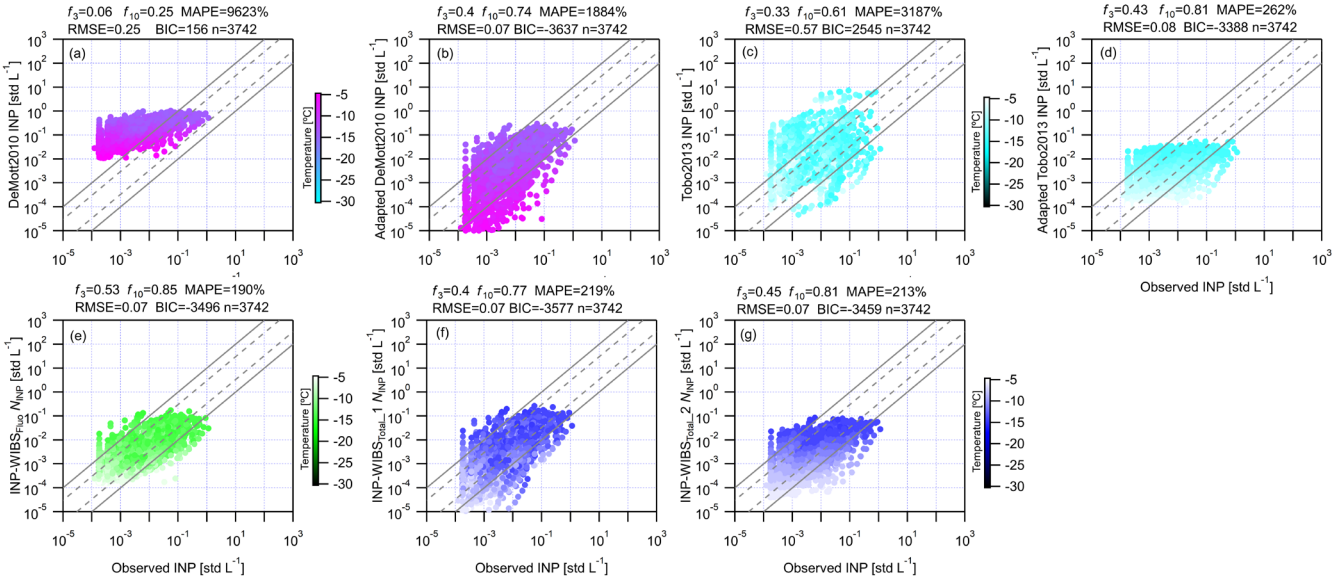

Figure 9. Comparisons of the performance of different parameterizations in Table 1 for data at $T \geq -15$°C. (a) DeMott2010. (b) Adapted DeMott2010 using a new set of parameters calculated by fitting the formula to the observed data. (c) Tobo2013. (d) Adapted Tobo2013 using a new set of parameters calculated by fitting the formula to the observed data. (e) WIBS$_{Fluo}$. (f) WIBS$_{Total}$_1. (g) WIBS$_{Total}$_2. The temperature condition for INP data is scaled to the color bar. Note that parameterizations using the same parameterization formula use the same color bar. The dashed lines confine the range for observed and predicted data points within a factor of 3. The fraction of observed and predicted data points within a factor of 3 (f_3) and 10 (f_{10}) is provided in each panel, respectively. MAPE stands for mean absolute percentage error. RMSE is the root-mean-square error used as a measure of the difference between observed and predicted data. BIC is a value calculated by applying the Bayesian information criteria to evaluate the goodness of parameterizations based on the same dataset (Schwarz, 1978). The *n* value shows the number of observed data points.

4 Conclusion

In this study, we investigate the role of different types of aerosols in MPC formation through field observations at a semi-rural site on the Swiss Plateau using INP and aerosol measurements, remote sensing, and air mass source analysis. The observed immersion-mode INPs (>−24°C) mainly originate from biological particles (>85%) - represented by fluorescent biological aerosols particles (FBAPs) - and pollen, followed by heat-resistant particles (<10%) like dust (Figs. 3 to 7). Notably, some pollen species may outperform the others (Fig. 4). Precipitation reduces INPs by removing smaller-sized FBAPs (<2.5µm, Supplement S10). We further developed and validated a bioaerosol-aware INP parameterization that

https://doi.org/10.5194/egusphere-2026-2699
Preprint. Discussion started: 29 May 2026

captures mixed biological–dust sources and outperforms existing ones across three field datasets. These findings improve representation of biological aerosol–cloud interactions and reduce uncertainty in climate feedback.

Aerosol source apportionment identified three types of aerosols, including PBAPs, dust and biomass burning particles, that could contribute to INP. In the end, PBAPs are by far the most important contributors to immersion-mode INPs for $T \geq -24$°C (Fig. 4 and Fig. 5). We found that large-sized pollen particles >10.0 μm contribute to INPs between −16 and −21°C (Fig. 4 and Supplement Fig. S24 for $\text{Hirst}_{\text{Total}}$). INPs for even warmer *T*s (>−16°C) are more likely from smaller-sized FBAPs (Fig. 4) including bacteria, bacteria agglomerates and fungal spores (Petersson Sjögren et al., 2023; Stopelli et al., 2017; Lukas et al., 2022). Moreover, results from multiple methods for monitoring biological particles (fluorescent PBAPs monitored by WIBS, pollen particles monitored by Rapid-E and Hirst) suggested that specific biological particle species (e.g., $\text{Hirst}_{\text{Total}}$ pollen, Fig. 4) may be better INPs than others. However, the statistical results reveal a weak and insignificant role of dust and biomass burning aerosol particles (Fig. 4). In addition, INPs in 85% of the samples (or more) effectively lose their ability to nucleate ice after heating at 90°C (Fig. 5). This finding strongly demonstrated the primary role of biological particles or particles associated with heat-labile materials in the observed INPs(Li et al., 2023; O'sullivan et al., 2018). Heat-resistant INP particles from mineral dust are a minor contribution, but they may be enriched during intense dust episodes (Figs. 4 and 7). We also note that precipitation events may exert both wash-out and raindrop-splash effects, which can counteract each other (results in Figs. S10 and S11 and discussions in Supplement Text S10). In brief, PBAPs were proved to be dominant INP sources (>85% for T>−24°C) for MPCs in a site on the Swiss Plateau in different seasons, irrespective of the presence of dust.

We used FBAP number concentration and ratio to represent their importance as INP contributors and applied to INP parameterizations (Figs. 8 and 9), given that fluorescence can be linked to biological material from PBAPs or carried by a dust particle (Savage et al., 2017; Morrison et al., 2020). The parameterizations developed here explicitly considered INP contributions from dust and PBAPs and were demonstrated to outperform existing parametrizations for predicting INPs (Tobo et al., 2013; Demott et al., 2010) observed in different regions (Gao et al., 2024; Li et al., 2023), in particularly for immersion-mode INPs at T>−15°C (Fig. 9). As data on fluorescence and INP activity of aerosols continue to be collected, our formulations can be expanded to cover even more regions of the globe and with higher accuracy.

5 Limitations

As PBAP emission rate may increase in a warm climate (Lo and Levetin, 2007) and given the dominant role that PBAPs have on INPs under warm MPC conditions, they likely will have an even more important – yet still unconstrained – impact on cloud radiative and precipitation fields over continents, mountainous terrain and the water cycle downwind of such areas. The data presented here, together with the resulting improved INP parameterizations, are an important contribution to modelling and understanding how PBAPs shape precipitation and climate now and in the future. In addition, our results, together with reported similar studies in North America (Tobo et al., 2013; Cornwell et al., 2023), the Amazon (Prenni et al.,

https://doi.org/10.5194/egusphere-2026-2699
Preprint. Discussion started: 29 May 2026

2009; Whitehead et al., 2016), and the Arctic (Pereira Freitas et al., 2023), underscore the need for continued unravelling of the respective roles of PBAPs and dust in MPC formation, including the separate consideration of INPs from dust particles that contain biological materials may be an even more important driver of INPs than presented here, given that PBAPs that lack fluorescence or are not captured by our pollen monitors. However, when applying the parameterization presented here – it would be for all the biological particles in the simulation, therefore sources of bias would in the end be related by the different INP activity of FBAPs versus non-fluorescent INPs of biological origin.

Data availability. The data presented in this publication will be made available at https://www.doi.org/10.16904/envidat.710. The DOI link will be activated for public access upon acceptance of publication.

Supplement. The supplement related to this article is provided with Figs S1 to S31 and Tables S1 and S2. Supplementary text is also provided.

Author contributions. KG, AP, and AN initiated the conceptualization and investigation. KG, AP, RF, BCr, and BTB conducted data curation. KG, AN, and AP validated the methodology. KG and AN performed formal analysis. AN, AP, ZAK, BCr, and DL provided resources. KG wrote the original draft and prepared the figures, with contributions from MG for lidar plots and BCr for aerosol particles. AN supervised KG and contributed to the review and editing. All authors provided comments on the draft.

Competing interests. The authors declare that they have no conflict of interest.

Acknowledgements. We thank Dr. Andrea Baccarini for his help with logistics at the beginning of the field campaign. We also thank colleagues from Dr. Zamin Kanji's Ice Nucleation Lab for their help with accessibility when KG performs droplet freezing experiments. We grateful to the secretary office from Federal Office of Meteorology and Climatology MeteoSwiss (Payerne) for their support with accessing their facilities during the field campaign. Rob Modini and Nora Nowak from PSI are acknowledged for their help with the AE-33 and TCA measurements at the site.

Financial support. This research has been supported by the European Research Council PyroTRACH project (project ID 726165) funded from H2020-EU.1.1. (ERC), the Swiss National Science Foundation project 192292, Atmospheric Acidity Interactions with Dust and its Impacts (AAIDI), the "PANhellnfrastructure for Atmospheric Composition and climatE change" (MIS 5021516). AP and RF acknowledge funding by the Basic Research Program PEVE (NTUA) under contract PEVE0011/2021. ZAK and CZ received financial support through the ACTRIS Switzerland 2025-2028 grant (Swiss contribution to the ACTRIS ERIC) funded by the Swiss State Secretariat for Education and Research and Innovation (SERI).

https://doi.org/10.5194/egusphere-2026-2699
Preprint. Discussion started: 29 May 2026

References

Augustin, S., Wex, H., Niedermeier, D., Pummer, B., Grothe, H., Hartmann, S., Tomsche, L., Clauss, T., Voigtländer, J., Ignatius, K., and Stratmann, F.: Immersion freezing of birch pollen washing water, Atmos. Chem. Phys., 13, 10989-11003, https://doi.org/10.5194/acp-13-10989-2013, 2013.

Beall, C. M., Lucero, D., Hill, T. C., DeMott, P. J., Stokes, M. D., and Prather, K. A.: Best practices for precipitation sample storage for offline studies of ice nucleation in marine and coastal environments, Atmos. Meas. Tech., 13, 6473-6486, https://doi.org/10.5194/amt-13-6473-2020, 2020.

Brunner, C., Brem, B. T., Collaud Coen, M., Conen, F., Hervo, M., Henne, S., Steinbacher, M., Gysel-Beer, M., and Kanji, Z. A.: The contribution of Saharan dust to the ice-nucleating particle concentrations at the High Altitude Station Jungfraujoch (3580 m a.s.l.), Switzerland, Atmos. Chem. Phys., 21, 18029-18053, https://doi.org/10.5194/acp-21-18029-2021, 2021.

Chappuis, C., Tummon, F., Clot, B., Konzelmann, T., Calpini, B., and Crouzy, B.: Automatic pollen monitoring: first insights from hourly data, Aerobiologia, 36, 159-170, https://doi.org/10.1007/s10453-019-09619-6, 2019.

Chatziparaschos, M., Myriokefalitakis, S., Kalivitis, N., Daskalakis, N., Nenes, A., Gonçalves Ageitos, M., Costa-Surós, M., Pérez García-Pando, C., Vrekoussis, M., and Kanakidou, M.: Assessing the global contribution of marine aerosols, terrestrial bioaerosols, and desert dust to ice-nucleating particle concentrations, Atmos. Chem. Phys., 25, 9085-9111, https://doi.org/10.5194/acp-25-9085-2025, 2025.

Coluzza, I., Creamean, J., Rossi, M., Wex, H., Alpert, P., Bianco, V., Boose, Y., Dellago, C., Felgitsch, L., Fröhlich-Nowoisky, J., Herrmann, H., Jungblut, S., Kanji, Z., Menzl, G., Moffett, B., Moritz, C., Mutzel, A., Pöschl, U., Schauperl, M., Scheel, J., Stopelli, E., Stratmann, F., Grothe, H., and Schmale, D.: Perspectives on the Future of Ice Nucleation Research: Research Needs and Unanswered Questions Identified from Two International Workshops, Atmos., 8, https://doi.org/10.3390/atmos8080138, 2017.

Conen, F., Einbock, A., Mignani, C., and Hüglin, C.: Measurement report: Ice-nucleating particles active ≥ -15 °C in free tropospheric air over western Europe, Atmos. Chem. Phys., 22, 3433-3444, https://doi.org/10.5194/acp-22-3433-2022, 2022.

Cornwell, G. C., McCluskey, C. S., Hill, T. C. J., Levin, E. T., Rothfuss, N. E., Tai, S.-L., Petters, M. D., DeMott, P. J., Kreidenweis, S., Prather, K. A., and Burrows, S. M.: Bioaerosols are the dominant source of warmtemperature immersion-mode INPs and drive uncertainties in INP predictability, Sci. Adv., 9, https://doi.org/10.1126/sciadv.adg3715, 2023.

Crouzy, B., Stella, M., Konzelmann, T., Calpini, B., and Clot, B.: All-optical automatic pollen identification: Towards an operational system, Atmos. Environ., 140, 202-212, https://doi.org/10.1016/j.atmosenv.2016.05.062, 2016.

D'Amico, G., Amodeo, A., Mattis, I., Freudenthaler, V., and Pappalardo, G.: EARLINET Single Calculus Chain – technical – Part 1: Pre-processing of raw lidar data, Atmos. Meas. Tech., 9, 491-507, https://doi.org/10.5194/amt-9-491-2016, 2016.

David, R. O., Cascajo-Castresana, M., Brennan, K. P., Rösch, M., Els, N., Werz, J., Weichlinger, V., Boynton, L. S., Bogler, S., Borduas-Dedekind, N., Marcolli, C., and Kanji, Z. A.: Development of the DRoplet Ice Nuclei Counter Zurich (DRINCZ): Validation and Application to Field-Collected Snow Samples, Atmos. Meas. Tech., 12, 6865-6888, https://doi.org/10.5194/amt-12-6865-2019, 2019.

DeMott, P. J., Prenni, A. J., Liu, X., Kreidenweis, S. M., Petters, M. D., Twohy, C. H., Richardson, M. S., Eidhammer, T., and Rogers, D. C.: Predicting global atmospheric ice nuclei distributions and their impacts on climate, Proc. Natl. Acad. Sci. U.S.A., 107, 11217-11222, https://doi.org/10.1073/pnas.0910818107, 2010.

Draxler, R. R. and Hess, G. D.: An Overview of the HYSPLIT_4 Modelling System for Trajectories, Dispersion, and Deposition, Aust. Meteorol. Mag., 47, 295-308, 1998.

Fröhlich-Nowoisky, J., Hill, T. C. J., Pummer, B. G., Yordanova, P., Franc, G. D., and Pöschl, U.: Ice nucleation activity in the widespread soil fungus Mortierella alpina, Biogeosciences, 12, 1057-1071, https://doi.org/10.5194/bg-12-1057-2015, 2015.

Gao, K., Vogel, F., Foskinis, R., Vratolis, S., Gini, M. I., Granakis, K., Billault-Roux, A.-C., Georgakaki, P., Zografou, O., Fetfatzis, P., Berne, A., Papagiannis, A., Eleftheridadis, K., Möhler, O., and Nenes, A.: Biological and dust aerosol as sources of ice nucleating particles in the Eastern Mediterranean: source apportionment, atmospheric processing and parameterization, Atmos. Chem. Phys., 24, 9939-9974, https://doi.org/10.5194/acp-24-9939-2024, 2024.

Georgakaki, P., Billault-Roux, A.-C., Foskinis, R., Gao, K., Sotiropoulou, G., Gini, M., Takahama, S., Eleftheriadis, K., Papayannis, A., Berne, A., and Nenes, A.: Unraveling secondary ice production in winter orographic clouds through a

https://doi.org/10.5194/egusphere-2026-2699
Preprint. Discussion started: 29 May 2026

synergy of in-situ observations, remote sensing and modeling, npj Clim. Atmos. Sci., 7, https://doi.org/10.1038/s41612-024-00671-9, 2024.

Gidarakou, M., Papayannis, A., Gao, K., Gidarakos, P., Crouzy, B., Foskinis, R., Erb, S., Zhang, C., Lieberherr, G., Coen, M. C., Branko, S., Kanji, Z. A., Clot, B., Calpini, B., Giagka, E., and Nenes, A.: Profiling pollen and biomass burning particles over Payerne, Switzerland using laser-induced fluorescence lidar and in situ techniques during the 2023 PERICLES campaign, Atmos. Chem. Phys., 26, 923-945, https://doi.org/10.5194/acp-26-923-2026, 2026.

Hill, T. C. J., DeMott, P. J., Tobo, Y., Fröhlich-Nowoisky, J., Moffett, B. F., Franc, G. D., and Kreidenweis, S. M.: Sources of organic ice nucleating particles in soils, Atmos. Chem. Phys., 16, 7195-7211, https://doi.org/10.5194/acp-16-7195-2016, 2016.

Hirst, J. M.: An Automatic Volumetric Spore Trap, Ann. Appl. Biol., 39, https://doi.org/10.1111/j.1744-7348.1952.tb00904.x, 1952.

Hoose, C., Kristjánsson, J. E., and Burrows, S. M.: How important is biological ice nucleation in clouds on a global scale?, Environ. Res. Lett., 5, https://doi.org/10.1088/1748-9326/5/2/024009, 2010.

Huffman, J. A., Prenni, A. J., DeMott, P. J., Pöhlker, C., Mason, R. H., Robinson, N. H., Fröhlich-Nowoisky, J., Tobo, Y., Després, V. R., Garcia, E., Gochis, D. J., Harris, E., Müller-Germann, I., Ruzene, C., Schmer, B., Sinha, B., Day, D. A., Andreae, M. O., Jimenez, J. L., Gallagher, M., Kreidenweis, S. M., Bertram, A. K., and Pöschl, U.: High concentrations of biological aerosol particles and ice nuclei during and after rain, Atmos. Chem. Phys., 13, 6151-6164, https://doi.org/10.5194/acp-13-6151-2013, 2013.

Kanji, Z. A., Welti, A., Corbin, J. C., and Mensah, A. A.: Black Carbon Particles Do Not Matter for Immersion Mode Ice Nucleation, Geophys. Res. Lett., 46, https://10.1029/2019gl086764, 2020.

Kanji, Z. A., Ladino, L. A., Wex, H., Boose, Y., Burkert-Kohn, M., Cziczo, D. J., and Krämer, M.: Overview of ice nucleating particles, in: Meteorological Monographs, 1.1-1.33, https://doi.org/10.1175/amsmonographs-d-16-0006.1, 2017.

Kiselev, D., Bonacina, L., and Wolf, J.-P.: Individual bioaerosol particle discrimination by multi-photon excited fluorescence, Opt. Express, 19, 24516-24521, https://doi.org/10.1364/OE.19.024516, 2011.

Kiselev, D., Bonacina, L., and Wolf, J. P.: A flash-lamp based device for fluorescence detection and identification of individual pollen grains, Rev. Sci. Instrum., 84, 033302, https://doi.org/10.1063/1.4793792, 2013.

Korolev, A. and Leisner, T.: Review of experimental studies of secondary ice production, Atmos. Chem. Phys., 20, 11767-11797, https://doi.org/10.5194/acp-20-11767-2020, 2020.

Korolev, A. and Milbrandt, J.: How Are Mixed-Phase Clouds Mixed?, Geophys. Res. Lett., 49, e2022GL099578, https://10.1029/2022GL099578, 2022.

Lacher, L., Clemen, H.-C., Shen, X., Mertes, S., Gysel-Beer, M., Moallemi, A., Steinbacher, M., Henne, S., Saathoff, H., Möhler, O., Höhler, K., Schiebel, T., Weber, D., Schrod, J., Schneider, J., and Kanji, Z. A.: Sources and nature of ice-nucleating particles in the free troposphere at Jungfraujoch in winter 2017, Atmos. Chem. Phys., https://doi.org/10.5194/acp-21-16925-2021, 2021.

Li, G., Wieder, J., Pasquier, J. T., Henneberger, J., and Kanji, Z. A.: Predicting atmospheric background number concentration of ice nucleating particles in the Arctic, Atmospheric Chemistry and Physics Discussions, https://doi.org/10.5194/acp-2022-21, 2022.

Li, G., Wilbourn, E. K., Cheng, Z., Wieder, J., Fagerson, A., Henneberger, J., Motos, G., Traversi, R., Brooks, S. D., Mazzola, M., China, S., Nenes, A., Lohmann, U., Hiranuma, N., and Kanji, Z. A.: Physicochemical characterization and source apportionment of Arctic ice-nucleating particles observed in Ny-Ålesund in autumn 2019, Atmos. Chem. Phys., 23, 10489-10516, https://doi.org/10.5194/acp-23-10489-2023, 2023.

Lo, E. and Levetin, E.: Influence of Meteorological Conditions on Early Spring Pollen in the Tulsa Atmosphere from 1987-2006, J. Allergy Clin. Immunol., 119, https://doi.org/10.1016/j.jaci.2006.11.612, 2007.

Lohmann, U.: A glaciation indirect aerosol effect caused by soot aerosols, Geophys. Res. Lett., 29, 11-11-11-14, https://doi.org/10.1029/2001GL014357, 2002.

Lohmann, U., Henneberger, J., Henneberg, O., Fugal, J. P., Bühl, J., and Kanji, Z. A.: Persistence of orographic mixed-phase clouds, Geophys. Res. Lett., 43, https://doi.org/10.1002/2016gl071036, 2016.

Lukas, M., Schwidetzky, R., Eufemio, R. J., Bonn, M., and Meister, K.: Toward Understanding Bacterial Ice Nucleation, J. Phys. Chem. B, 126, 1861-1867, https://doi.org/10.1021/acs.jpcb.1c09342, 2022.

https://doi.org/10.5194/egusphere-2026-2699
Preprint. Discussion started: 29 May 2026

Mattis, I., D'Amico, G., Baars, H., Amodeo, A., Madonna, F., and Iarlori, M.: EARLINET Single Calculus Chain – technical – Part 2: Calculation of optical products, Atmos. Meas. Tech., 9, 3009-3029, https://doi.org/10.5194/amt-9-3009-2016, 2016.
McCoy, D. T., Tan, I., Hartmann, D. L., Zelinka, M. D., and Storelvmo, T.: On the relationships among cloud cover, mixed-phase partitioning, and planetary albedo in GCMs, Journal of Advances in Modeling Earth Systems, 8, 650-668, https://doi.org/10.1002/2015ms000589, 2016.
Morrison, D., Crawford, I., Marsden, N., Flynn, M., Read, K., Neves, L., Foot, V., Kaye, P., Stanley, W., Coe, H., Topping, D., and Gallagher, M.: Quantifying bioaerosol concentrations in dust clouds through online UV-LIF and mass spectrometry measurements at the Cape Verde Atmospheric Observatory, Atmos. Chem. Phys., 20, 14473-14490, https://10.5194/acp-20-14473-2020, 2020.
Morrison, H., de Boer, G., Feingold, G., Harrington, J., Shupe, M. D., and Sulia, K.: Resilience of persistent Arctic mixed-phase clouds, Nat. Geosci., 5, 11-17, https://doi.org/10.1038/ngeo1332, 2011.
Mülmenstädt, J., Salzmann, M., Kay, J. E., Zelinka, M. D., Ma, P.-L., Nam, C., Kretzschmar, J., Hörnig, S., and Quaas, J.: An underestimated negative cloud feedback from cloud lifetime changes, Nature Climate Change, 11, 508-513, https://doi.org/10.1038/s41558-021-01038-1, 2021.
Murray, B. J., O'Sullivan, D., Atkinson, J. D., and Webb, M. E.: Ice Nucleation by Particles Immersed in Supercooled Cloud Droplets, Chem. Soc. Rev., 41, 6519-6554, https://doi.org/10.1039/c2cs35200a, 2012.
Murray, K. A., Kinney, N. L. H., Griffiths, C. A., Hasan, M., Gibson, M. I., and Whale, T. F.: Pollen derived macromolecules serve as a new class of ice-nucleating cryoprotectants, Sci Rep, 12, 12295, https://doi.org/10.1038/s41598-022-15545-4, 2022.
O'Sullivan, D., Murray, B. J., Malkin, T. L., Webb, M. E., Whale, T. F., Atkinson, J. D., and Baustian, K. J.: Atmospheric ice nucleation by fertile soil dusts particles: Relative importance of mineral and biological components, https://doi.org/10.1063/1.4803409, 2013.
O'Sullivan, D., Adams, M. P., Tarn, M. D., Harrison, A. D., Vergara-Temprado, J., Porter, G. C. E., Holden, M. A., Sanchez-Marroquin, A., Carotenuto, F., Whale, T. F., McQuaid, J. B., Walshaw, R., Hedges, D. H. P., Burke, I. T., Cui, Z., and Murray, B. J.: Contributions of biogenic material to the atmospheric ice-nucleating particle population in North Western Europe, Scientific Reports 8, 13821, https://doi.org/10.1038/s41598-018-31981-7, 2018.
Oteros, J., Buters, J., Laven, G., Röseler, S., Wachter, R., Schmidt-Weber, C., and Hofmann, F.: Errors in determining the flow rate of Hirst-type pollen traps, Aerobiologia, 33, 201-210, https://doi.org/10.1007/s10453-016-9467-x, 2016.
Oteros, J., Buters, J., Laven, G., Röseler, S., Wachter, R., Schmidt-Weber, C., and Hofmann, F.: Errors in determining the flow rate of Hirst-type pollen traps, Aerobiologia, 33, 201-210, https://doi.org/10.1007/s10453-016-9467-x, 2017.
Patade, S., Waman, D., Deshmukh, A., Gupta, A. K., Jadav, A., Phillips, V. T. J., Bansemer, A., Carlin, J., and Ryzhkov, A.: The influence of multiple groups of biological ice nucleating particles on microphysical properties of mixed-phase clouds observed during MC3E, Atmos. Chem. Phys., 22, 12055-12075, https://doi.org/10.5194/acp-22-12055-2022, 2022.
Patnaude, R. J., McCluskey, C. S., Roberts, G. C., DeMott, P. J., Hill, T. C. J., McFarquhar, G. M., Kollias, P., Ranjbar, K., Wolde, M., and Kreidenweis, S. M.: Characteristics of Ice Nucleating Particles From the Long-Range Transport of Saharan Dust, Geophys. Res. Lett., 52, https://doi.org/10.1029/2024gl113365, 2025.
Pereira Freitas, G., Adachi, K., Conen, F., Heslin-Rees, D., Krejci, R., Tobo, Y., Yttri, K. E., and Zieger, P.: Regionally sourced bioaerosols drive high-temperature ice nucleating particles in the Arctic, Nat. Commun., 14, 5997, https://doi.org/10.1038/s41467-023-41696-7, 2023.
Perring, A. E., Schwarz, J. P., Baumgardner, D., Hernandez, M. T., Spracklen, D. V., Heald, C. L., Gao, R. S., Kok, G., McMeeking, G. R., McQuaid, J. B., and Fahey, D. W.: Airborne observations of regional variation in fluorescent aerosol across the United States, J. Geophys. Res. Atmos., 120, 1153-1170, https://doi.org/10.1002/2014jd022495, 2015.
Petersson Sjögren, M., Alsved, M., Šantl-Temkiv, T., Bjerring Kristensen, T., and Löndahl, J.: Measurement report: Atmospheric fluorescent bioaerosol concentrations measured during 18 months in a coniferous forest in the south of Sweden, Atmos. Chem. Phys., 23, 4977-4992, https://doi.org/10.5194/acp-23-4977-2023, 2023.
Petters, M. D. and Wright, T. P.: Revisiting ice nucleation from precipitation samples, Geophys. Res. Lett., 42, 8758-8766, https://doi.org/10.1002/2015gl065733, 2015.
Phillips, V. T. J., Yano, J.-I., and Khain, A.: Ice Multiplication by Breakup in Ice–Ice Collisions. Part I: Theoretical Formulation, J. Atmos. Sci., 74, 1705-1719, https://doi.org/10.1175/jas-d-16-0224.1, 2017.

https://doi.org/10.5194/egusphere-2026-2699
Preprint. Discussion started: 29 May 2026

Prenni, A. J., Petters, M. D., Kreidenweis, S. M., Heald, C. L., Martin, S. T., Artaxo, P., Garland, R. M., Wollny, A. G., and Pöschl, U.: Relative roles of biogenic emissions and Saharan dust as ice nuclei in the Amazon basin, Nat. Geosci., 2, 402-405, https://doi.org/10.1038/ngeo517, 2009.

Pruppacher, H. R. and Klett, J. D.: Microphysics of Clouds and Precipitation, Atmospheric and Oceanographic Sciences Library, Kluwer, Dordrecht2010.

Rigler, M., Drinovec, L., Lavrič, G., Vlachou, A., Prévôt, A. S. H., Jaffrezo, J. L., Stavroulas, I., Sciare, J., Burger, J., Kranjc, I., Turšič, J., Hansen, A. D. A., and Močnik, G.: The new instrument using a TC–BC (total carbon–black carbon) method for the online measurement of carbonaceous aerosols, Atmos. Meas. Tech., 13, 4333-4351, https://doi.org/10.5194/amt-13-4333-2020, 2020.

Šaulienė, I., Šukienė, L., Daunys, G., Valiulis, G., Vaitkevičius, L., Matavulj, P., Brdar, S., Panic, M., Sikoparija, B., Clot, B., Crouzy, B., and Sofiev, M.: Automatic pollen recognition with the Rapid-E particle counter: the first-level procedure, experience and next steps, Atmos. Meas. Tech., 12, 3435-3452, https://doi.org/10.5194/amt-12-3435-2019, 2019.

Savage, N. J., Krentz, C. E., Könemann, T., Han, T. T., Mainelis, G., Pöhlker, C., and Huffman, J. A.: Systematic characterization and fluorescence threshold strategies for the wideband integrated bioaerosol sensor (WIBS) using size-resolved biological and interfering particles, Atmos. Meas. Tech., 10, 4279-4302, https://doi.org/10.5194/amt-10-4279-2017, 2017.

Schneider, J., Höhler, K., Heikkilä, P., Keskinen, J., Bertozzi, B., Bogert, P., Schorr, T., Umo, N. S., Vogel, F., Brasseur, Z., Wu, Y., Hakala, S., Duplissy, J., Moisseev, D., Kulmala, M., Adams, M. P., Murray, B. J., Korhonen, K., Hao, L., Thomson, E. S., Castarède, D., Leisner, T., Petäjä, T., and Möhler, O.: The seasonal cycle of ice-nucleating particles linked to the abundance of biogenic aerosol in boreal forests, Atmos. Chem. Phys., 21, 3899-3918, https://doi.org/10.5194/acp-21-3899-2021, 2021.

Schwarz, G.: Estimating the Dimension of a Model, The Annals of Statistics, 6, 461-461, https://doi.org/10.1214/aos/1176344136, 1978.

Standardization, E. C. f., EN 16868:2019 — Ambient air: Sampling and analysis of airborne pollen grains and fungal spores for networks related to allergy — Volumetric Hirst method, Rule number, 2019.

Stein, A. F., Draxler, R. R., Rolph, G. D., Stunder, B. J. B., Cohen, M. D., and Ngan, F.: NOAA's HYSPLIT Atmospheric Transport and Dispersion Modeling System, Bull. Am. Meteorol. Soc., 96, 2059-2077, https://doi.org/10.1175/bams-d-14-00110.1, 2015.

Steinke, I., Funk, R., Busse, J., Iturri, A., Kirchen, S., Leue, M., Möhler, O., Schwartz, T., Schnaiter, M., Sierau, B., Toprak, E., Ullrich, R., Ulrich, A., Hoose, C., and Leisner, T.: Ice nucleation activity of agricultural soil dust aerosols from Mongolia, Argentina, and Germany, J. Geophys. Res. Atmos., 121, https://doi.org/10.1002/2016jd025160, 2016.

Stopelli, E., Conen, F., Guilbaud, C., Zopfi, J., Alewell, C., and Morris, C. E.: Ice nucleators, bacterial cells and Pseudomonas syringae in precipitation at Jungfraujoch, Biogeosciences, 14, 1189-1196, https://doi.org/10.5194/bg-14-1189-2017, 2017.

Suski, K. J., Hill, T. C. J., Levin, E. J. T., Miller, A., DeMott, P. J., and Kreidenweis, S. M.: Agricultural harvesting emissions of ice-nucleating particles, Atmos. Chem. Phys., 18, 13755-13771, https://doi.org/10.5194/acp-18-13755-2018, 2018.

Tang, D., Wei, T., Yuan, J., Xia, H., and Dou, X.: Observation of bioaerosol transport using wideband integrated bioaerosol sensor and coherent Doppler lidar, Atmos. Meas. Tech., 15, 2819-2838, https://doi.org/10.5194/amt-15-2819-2022, 2022.

Tešendić, D., Boberić Krstićev, D., Matavulj, P., Brdar, S., Panić, M., Minić, V., and Šikoparija, B.: RealForAll: real-time system for automatic detection of airborne pollen, Enterprise Information Systems, 16, https://doi.org/10.1080/17517575.2020.1793391, 2020.

Tobo, Y., Prenni, A. J., DeMott, P. J., Huffman, J. A., McCluskey, C. S., Tian, G., Pöhlker, C., Pöschl, U., and Kreidenweis, S. M.: Biological aerosol particles as a key determinant of ice nuclei populations in a forest ecosystem, J. Geophys. Res. Atmos., 118, 10,100-110,110, https://doi.org/10.1002/jgrd.50801, 2013.

Veselovskii, I., Hu, Q., Goloub, P., Podvin, T., Korenskiy, M., Pujol, O., Dubovik, O., and Lopatin, A.: Combined use of Mie–Raman and fluorescence lidar observations for improving aerosol characterization: feasibility experiment, Atmos. Meas. Tech., 13, 6691-6701, https://doi.org/10.5194/amt-13-6691-2020, 2020.

https://doi.org/10.5194/egusphere-2026-2699
Preprint. Discussion started: 29 May 2026

Whitehead, J. D., Darbyshire, E., Brito, J., Barbosa, H. M. J., Crawford, I., Stern, R., Gallagher, M. W., Kaye, P. H., Allan, J. D., Coe, H., Artaxo, P., and McFiggans, G.: Biogenic cloud nuclei in the central Amazon during the transition from wet to dry season, Atmos. Chem. Phys., 16, 9727-9743, https://doi.org/10.5194/acp-16-9727-2016, 2016.

Wieder, J., Mignani, C., Schär, M., Roth, L., Sprenger, M., Henneberger, J., Lohmann, U., Brunner, C., and Kanji, Z. A.: Unveiling atmospheric transport and mixing mechanisms of ice-nucleating particles over the Alps, Atmos. Chem. Phys., 22, 3111-3130, https://doi.org/10.5194/acp-22-3111-2022, 2022.